Physics of Fluids ARTICLE pubs.aip.org/aip/pof

Linear stability analysis of second-mode attenuation via porous carbon-matrix ceramics

Cite as: Phys. Fluids **35**, 064113 (2023); doi: 10.1063/5.0152894
Submitted: 2 April 2023 · Accepted: 29 May 2023 ·
Published Online: 14 June 2023

Victor C. B. Sousa,[1,a)] Viola Wartemann,[2] Alexander Wagner,[2] and Carlo Scalo[1,3]

AFFILIATIONS

[1]School of Mechanical Engineering, Purdue University, West Lafayette, Indiana 47907, USA
[2]German Aerospace Center (DLR), Institute of Aerodynamics and Flow Technology, Göttingen 37073, Germany
[3]School of Aeronautical and Astronautical Engineering, Purdue University, West Lafayette, Indiana 47907, USA

[a)]Author to whom correspondence should be addressed: vsousa@purdue.edu

ABSTRACT

Effects of porous carbon-fiber-reinforced carbon-matrix ceramics (C/C) on the stability of second-mode waves on a 7°-half-angle cone were investigated for Reynolds numbers $Re_m = 2.43 \times 10^6$–6.40×10^6 m^{-1} at the freestream Mach number of $M_\infty = 7.4$, for both sharp and 2.5-mm-round nose tips. A broadband time-domain impedance boundary condition was used to model the effects of the C/C porosity on the flow dynamics leveraging direct ultrasonic benchtop experiments and homogenous absorber theory. A spectral linear stability solver based on orthogonal Laguerre functions, naturally vanishing in the free stream, was used to predict linear spatial growth rates, which are in agreement with independent pulsed axisymmetric direct-numerical simulations. The latter were carried out with the quasi-spectral viscosity closure—a dynamic quasi-spectral procedure capable of deactivating the sub-filter scale stresses in the absence of turbulent break down—verifying its suitability to carry out transitional calculations without affecting ultrasonic wave dynamics. The effectiveness of a porous C/C surface is shown to decrease drastically with static pressure and its presence is shown to decrease the second-mode growth rates in regions where it is unstable as well as increasing the attenuation rates in regions where it is stable.

I. INTRODUCTION

Implications of laminar-to-turbulent transition are critical for the design, performance, and safe operation of hypersonic vehicles. Turbulent flow conditions entail dramatic increases in wall-heat flux and friction with respect to laminar conditions (Schneider, 2004), making any technology capable of delaying hypersonic laminar-to-turbulent transition very attractive.

Disturbances in a boundary layer over smooth surfaces, slender bodies, and in low-disturbance environments may be initiated by free stream fluctuations (Fedorov, 2003). This receptivity process is typically followed by modal growth, which is accurately captured by a linear stability theory (LST) (Morkovin *et al.*, 1994; Fedorov, 2011). A compressible boundary layer exhibits multiple instabilities across the frequency spectrum. As the Mach number (M) increases, the second unstable region (ordered by frequency) becomes more significant and, at a certain point, Mack's second-modal instability becomes predominant, especially in the presence of cooled walls ($T_w < T_{adb}$) (Mack, 1984; 1969). Mack's research on these modal instabilities in two-dimensional boundary layers (Mack, 1990) demonstrated the importance of attenuating the second-mode when transition delay in high-speed flows is desired. Moreover, Fedorov and Tumin (2011) have shown that the second-mode instability and its higher frequency counterparts are associated with the branching of the fast (F) and slow (S) modes near their synchronization. The corresponding modes are named after the fast $(1 + 1/M)$ and slow $(1 - 1/M)$ acoustic waves that are asymptotically approached near the origin of a boundary layer. Although Fedorov and Tumin (2011) argue that this terminology is more mathematically appropriate, especially for boundary layer receptivity studies, they also recognize that the use of Mack's original terminology for the interpretation of the experimental data and LST results is reasonable.

Using a LST-based analysis, Malmuth *et al.* (1998) showed that ultrasonically absorbing coatings (UACs) can be used to mitigate the second-mode. Experiments conducted in the T-5 hypersonic wind tunnel at Caltech (Fedorov *et al.*, 2001; Rasheed *et al.*, 2002) at Mach 5 on a cone with a half angle of 5° with two different surfaces (smooth and impermeable, as well as perforated with regularly spaced micro holes) provided the first experimental validation of this principle. Results indicated that the porous surface was able to double the transitional Reynolds number compared to the smooth surface.

Experiments conducted by Fedorov *et al.* (2003; 2006) in the Mach 6 wind tunnel, T-326 at the Institute of Theoretical and Applied Mechanics (ITAM) in Novosibirsk, aimed to test surfaces that could combine acoustic absorption and thermal protection system (TPS) characteristics into one solution. The experiments, which were conducted over a porous surface with regular microstructure and over a felt-metal surface, quantitatively demonstrated the attenuation of the second-mode waves via UACs. A subsequent correction of an error in the stability analysis performed by Fedorov *et al.* (2003) and Tritarelli *et al.* (2015) confirmed the presence of a shift of second-mode instabilities to lower frequencies over felt-metal porous structures.

Moreover, Lukashevich *et al.* (2016) also conducted experiments in ITAM's tunnel, which revealed that when the porous insert was placed in a region where the growth rate of the second-mode instability was expected to be negative, the disturbance signal amplitude increased; however, if it was situated in an area of positive growth rate, the opposite was observed. Additionally, Morozov *et al.* (2018) examined the angle of attack effects with $\alpha < 1^\circ$ and determined that the porous coating could reduce second-mode disturbances whether they were on the windward or leeward sides of the cone.

Motivated by some of these findings and the need for a feasible technology for boundary layer control that works in harmony with TPS, Wagner *et al.* (2013) introduced the second-mode waves controlling use of porous carbon–carbon (C/C), an intermediary state of C/C Silicon Carbide (C/C-SiC) that was already utilized on hypersonic vehicles (Turner *et al.*, 2006; Weihs *et al.*, 2008). Experimental validation on the effectiveness of C/C-based porous surfaces in achieving transition delay was achieved through tests conducted at approximately Mach 7.5 in the German Aerospace Center (DLR) High Enthalpy Shock Tunnel Göttingen (HEG). An attenuation of the second-modal instability as well as an increase in the laminar portion of the boundary layer over the porous surface were observed. For these flow conditions, Wartemann *et al.* (2015) conducted an analysis using parabolized stability equations, which provided further evidence on the effectiveness of C/C-based porous surfaces decreasing the growth rate of the unstable modes present in the boundary layer.

A similar C/C surface was used in a 3° half angle sharp cone on different experimental runs in a conventional and a quiet wind tunnel at Mach 6. Willems *et al.* (2017) performed experiments in the Boeing/AFOSR Mach-6 Quiet Tunnel (BAM6QT) at Purdue University and in the hypersonic wind tunnel (H2K) of the German Aerospace Center (DLR) in Cologne and reported no significant attenuation or transition delay over the porous surfaces. Early modeling work by Sousa *et al.* (2019) infers that the reason for this comes from the flow conditions chosen for the study, which entailed very low pressures on the model's surface and low-frequency second-mode waves (lower than 150 kHz). A linear stability analysis of the flow conditions related to the experiments by Willems *et al.* (2017) was conducted and the results confirmed the decrease in effectiveness of the C/C porous surfaces when submitted to such environment. At these conditions, the porous carbon/carbon surface has low acoustic absorption capabilities. A careful impedance characterization of DLR's C/C material is included in the Appendix.

A more recent work on the effects of porous surfaces in hypersonic boundary layers was conducted by Zhu *et al.* (2020). A permeable steel material (PM-35) was included in the surface of a flared cone model and was studied both experimentally, with a focused laser differential interferometer (FLDI) methodology, and numerically, by modeling its impedance as a stack of staggered perforated rigid panels to study the stability of the flow in both linear and nonlinear regimes. The study concluded that the permeable wall suppresses disturbances in the boundary layer and scrambles the growth mechanism of secondary instabilities, ultimately delaying transition.

Most of the previous work on the numerical simulation of the influence of a porous surfaces of either regular or irregular structure on the stability boundary layers (Egorov *et al.*, 2008; Wang and Zhong, 2010; 2011; Lukashevich *et al.*, 2012) have focused on the effects of such a boundary condition on a single frequency component at a time. This is because they were based on an analytical relation introduced by Fedorov *et al.* (2001) which relates the wall-normal velocity and pressure fluctuations at the surface given a certain wall-normal impedance,

$$Z_n(\omega) = \frac{1}{\rho_0 a_0} \frac{\hat{p}(\omega)}{\hat{u}_n(\omega)}, \tag{1}$$

within the context of the single-frequency framework. Here, $\rho_0 a_0$ is the base impedance, ω is the angular frequency, and $\hat{u}_n$ and $\hat{p}$ are the Fourier transform of wall-normal velocity and pressure fluctuations, respectively.

Although this approach is perfectly suitable to study the linear stability characteristics of a boundary layer, one of the objectives of the current manuscript is to introduce a framework where simulations of the full transition path from laminar to turbulent of a hypersonic boundary layer over a porous surface can be conducted. In that case, the attenuation effects caused by wall-porosity need to be accounted for in a wide range of frequencies simultaneously. With that objective, the time domain impedance boundary condition (TDIBC) is used in this work due to its capability of applying broadband impedance effects to high-fidelity compressible flow simulations (Scalo *et al.*, 2015; Lin *et al.*, 2017; Douasbin *et al.*, 2018; Sousa *et al.*, 2019; Chen and Scalo, 2021b).

The current manuscript is dedicated to address three different aspects regarding numerical predictions concerning the influence of porous carbon-matrix ceramics on a hypersonic boundary layer. First, axisymmetric simulations of the experimental conditions reported in the transition delay experiments by Wagner *et al.* (2013) are conducted, and the second-mode instability attenuation characteristics of an impedance boundary condition representative of a porous carbon-matrix ceramics material is analyzed. The present effort is a significant improvement over the germinal work by Sousa *et al.* (2019), introducing a novel spectral approach to the linearized governing equations (Sec. III) to obtain spatial growth rates and compare against axisymmetric results as well as extends the scope of the study to both sharp- and blunt-nosed cones (Subsec. IV A). The current implementation of a LST solver used orthogonal functions on the positive half-plane that naturally display the exponentially decaying behavior observed in boundary layer unstable modes. In contrast, previous implementations based on finite differences (Malik, 1990; Kocian, 2018) require a boundary condition imposition at a finite distance away from the wall. Second, linear stability results for the experimental flow conditions reported by Willems *et al.* (2017) are studied and an explanation is given on the reason why transition delay was not observed in this separate on this separate experimental effort even though a similar C/C porous surface was used (Subsec. IV B). To the author's knowledge,

this is the most complete study on the impact of C/C porous surfaces on a hypersonic boundary layers to date.

The third, and final, objective of the current work is provide evidence that the current framework is suitable to conduct three-dimensional dynamic large-eddy simulations properly capturing the full transition path to turbulence, without spuriously attenuating instability waves. Within this goal, the high-fidelity simulations presented herein are executed with a sub-filter scale quasi-spectral viscosity (QSV) model developed in Sousa and Scalo (2022) which, despite not being necessary for the current axisymmetric runs, are expected to be essential for dissipating the steep gradients present upon breakdown to turbulence in hypersonic boundary layers and to decrease the resolution requirements on the fully turbulent region of the flow. For this goal to be achieved, the first step is to demonstrate that the QSV model is capable of dynamically deactivating itself, hence not affecting second-mode instability dynamics in the laminar portion of the flow. Ultimately, the numerical study here presented was conducted with sub-filter scale model active and agreement between the axisymmetric simulations and linear stability results was recovered (Subsec. IV A), showcasing QSV's suitability for three-dimensional transitional simulations.

II. PROBLEM FORMULATION

Axisymmetric time-resolved simulations of a conical flow over both impermeable and porous walls are conducted, inspired by the hypersonic boundary layer transition delay experiments performed by Wagner *et al.* (2013) in the DLR High Enthalpy Shock Tunnel Göttingen (HEG). The full details about the facility are reported in Hannemann *et al.* (2018). Table I reports the subset of experimental flow conditions that the current modeling effort will focus on.

Isothermal boundary conditions $T_w = 300$ K are imposed in both cases. This assumption closely represents the conditions at the surface of the conical model because the test duration is in the of the order of a few milliseconds and, despite the heat transfer rate being high at the wall, its time window is insufficient to provoke any significant temperature change on the solid surface.

A broadband time-domain impedance boundary condition (TDIBC) is used to model the influence of surface porosity over a wide range of frequencies relevant to both acoustic and hydrodynamic processes in compressible boundary layers (Scalo *et al.*, 2015; Chen and Scalo, 2021a). Contrary to the simple introduction of an impedance boundary condition in a linear stability solver, extra steps need to be taken to account for the effects of a complex-valued impedance in a Navier–Stokes solver. For the LST case, a frequency-by-frequency analysis suffices and one can simply apply Eq. (1) at the boundary. On the other hand, the currently developed time-domain solver is able to apply a broadband response by following the formalism introduced by Fung and Ju (2004), where the wall softness,

$$\hat{S}(\omega) = \frac{2}{1 + Z_n(\omega)}, \tag{2}$$

is approximated with a finite number of complex poles (p_k) and residues (μ_k). This quantity is chosen because it is finite as the frequency approaches zero and the impedance approaches infinity. Following, an inverse Laplace transform is applied and a representation of the wall softness as a function of time,

$$S(t) \approx \sum_{k=1}^{n_o} \left[\mu_k e^{p_k t} + \mu_k^* e^{p_k^* t}\right], \tag{3}$$

is achieved. From here, one can relate $S(t)$ with the incident and reflected waves from given surface and construct a causal convolution integral that can be numerically integrated to recover the correct velocity fluctuation that should be imposed given a certain complex impedance curve. To accurately represent a porous C/C surface in an impedance eduction step was performed (Appendix) and the curves were fitted via the vector fitting procedure outlined by Gustavsen and Semlyen (1999). Further details of the TDIBC can be found in publications by Scalo *et al.* (2015), Sousa *et al.* (2019), and Chen and Scalo (2021b).

A steady hypersonic base flow over a sharp cone at Reynolds numbers $Re_m = 2.43 \times 10^6\ \mathrm{m}^{-1}$ and $4.06 \times 10^6\ \mathrm{m}^{-1}$; and over a 2.5 mm blunt tip cone for $Re_m = 4.06 \times 10^6$ and $6.40 \times 10^6\ \mathrm{m}^{-1}$ is first obtained (Sec. IV A) and then perturbed via a one-time pulse. The resulting convective growth of the perturbation is then tracked. Despite temperatures in the hypersonic boundary layer peaking between 850 and 950 K (see Figs. 3 and 4), the current numerical studies have assumed a calorically perfect gas.

In the current work, the filtered Navier–Stokes equations written for a generalized set of curvilinear coordinates (Jordan 1999; Nagarajan *et al.* 2007) are discretized via a sixth-order Padé compact finite difference scheme (Lele, 1992) coupled with a third-order Runge–Kutta time integration method. As previously discussed, the simulations reported in the current manuscript were conducted with an active QSV sub-filter scale closure (Sousa and Scalo, 2022) in order to demonstrate its capability of dynamically modulating its strength and leaving the second-mode instability unaffected. This is discussed in Subsec. IV A, where growth rates predicted by a newly developed independent linear stability solver (Sec. III), match the ones recovered through the numerical simulations. The QSV model is able to perform this task because it leverages residuals of filter operations to estimate the energy of the resolved solution at the length scales in the vicinity of

TABLE I. Nominal flow parameters from Wagner *et al.* (2013). Throughout the paper, each of these flow conditions will be represented by the color/symbol here assigned.

Color/symbol	Re_m (1/m)	M_∞ (–)	p_∞ (Pa)	T_∞ (K)	ρ_∞ (kg/m^3)
Blue filled star	1.46×10^6	7.3	789	267	0.0102
Gray filled left triangle	2.43×10^6	7.4	1453	285	0.0177
Green filled circle	4.06×10^6	7.4	2129	268	0.0276
Black filled diamond	6.40×10^6	7.4	3083	248	0.0432
Red filled triangle	9.80×10^6	7.4	5174	265	0.0678

TABLE II. Streamwise extent (L_x) of the computational domain (Fig. 1) for the different flow conditions and cone geometries considered.

		Re_m		
L_x		$2.43 \times 10^6\ \mathrm{m}^{-1}$	$4.06 \times 10^6\ \mathrm{m}^{-1}$	$6.40 \times 10^6\ \mathrm{m}^{-1}$
R_{tip}	0.0 mm	0.8 m	0.6 m	⋯
	2.5 mm	⋯	0.9 m	0.8 m

the grid cutoff as well as concentrating the dissipation at the high-wavenumber part of the spectrum. The clever usage of filter's residuals gives the QSV model a combined capability of simulating shocks and turbulence either separately or concomitantly. Ultimately, it represents a unified model for shock capturing and Large-Eddy Simulation. Further details can be found in Sousa and Scalo (2022).

The initial conditions over the sharp cone geometry are obtained via a blend of the Taylor and Maccoll (1933) inviscid solution and a similarity solution for a compressible boundary layer over a cone Lees (1956). The blunt-nosed geometries is initialized by using data from a precursor simulation conducted with the DLR FLOWer code (Kroll and Fassbender, 2006). A small transient adjustment is observed due to the interpolation of the initial conditions onto the grid; after the solution is relaxed, excellent matching between the steady-state Navier–Stokes solution and the imposed initial conditions is recovered (Sec. IV A).

The inlet of the computational domain is located at $x_i = 0.045$ m from the sharp cone tip to avoid the stringent resolution requirements that would be necessary to solve the very thin boundary layer present in this region. The outlet is located at a distance of L_x (Table II) downstream of said inflow plane, as indicated in Fig. 1. The choice of L_x was made to reflect the minimum extent necessary to capture the full transition path to turbulence, for both impermeable and porous surface cases, in preparation for future three-dimensional calculations.

In the current effort the orthogonality constraint embedded in the spherical grid arrangement previously used in (Sousa *et al.*, 2019) was relaxed and the computational domain was restricted to the post shock region. The final grid setup is shown in Fig. 1. These choices allowed a more flexible concentration of points in the near-wall region and the decrease in the total number of points used in the wall normal direction without a loss in simulation accuracy.

The final grid arrangement can be analytically described by a combination of lines separating regions of different stretching laws in the x–y plane. The domain's upper boundary is described by a line that connects the locations $y_{i,\mathrm{top}} = 0.005$ m to $y_{o,\mathrm{top}} = 0.030$ m. Additionally, a line between another set of locations, $y_{i,\mathrm{int}} = 0.001$ m to $y_{o,\mathrm{int}} = 0.005$ m, is used to mark the boundary between regions of the computational space that contain the same number of grid points in the wall-normal direction. Separate stretching laws are used in these two regions: exponential in the near-wall and geometrical outside. The expansion ratio used in the geometrical stretching region was chosen at each streamwise location so that the grid points contained in this region covered extent between the intermediate line and the upper boundary. Finally, a Savitzky–Golay filter operation is performed to smoothen the discontinuity in the second derivative of the grid along the wall normal direction. This step ensures the smoothness of grid transformation metrics necessary to compute the flow dynamics in a generalized curvilinear grid (Jordan, 1999; Nagarajan *et al.*, 2007; Sousa and Scalo, 2022).

Dirichlet boundary conditions are imposed at the left and top boundaries matching the initial flow conditions. At the right boundary, homogeneous Neumann conditions are imposed for all conserved quantities. Sponge layers are used to either weakly impose inflow boundary conditions or to suppress flow fluctuations advecting downstream prior to their interaction with the outflow boundary. The left and right sponges' width is equal to $0.03L_x$, while the top boundary sponge is 5% of the local domain height. In all cases no-slip conditions, and either no penetration or a velocity fluctuation attached to an impedance boundary condition are imposed at the cone's surface. This approach bypasses the need to resolve the intricate pore geometry of a C/C-based porous surface, while still accurately modeling their acoustic effect on the overlying flow. On the other hand, it requires a separate surface impedance characterization, detailed in the Appendix.

III. SPECTRAL LINEAR STABILITY SOLVER

This section reports the development and verification of a linear stability solver based on a Laguerre spectral discretization. In addition to the exponential convergence rate inherent to a spectral discretization method, which is significantly faster than the fixed convergence rate observed in finite-difference schemes, another advantage of this approach is its natural suitability to problems with evanescing boundary conditions at infinity; for example, problems such as the stability of a boundary layer, of a vortex core, or perhaps even an of atom. This is due to the fact that the Laguerre functions, i.e., the orthogonal modes used to discretize the equations, are defined in the only for the positive real numbers including zero and exponentially decay at infinity. Shifting the focus to the problem at hand, since the unstable modes inside a boundary layer decay exponentially as they move further into the flow's free stream, this approach is able to naturally impose this condition without having to rely on an unphysical imposition of homogenous Dirichlet or Neumann condition at a finite distance off the wall. On the other hand, its greatest strength can become its weakness if this approach is used to discretize phenomena that are not clustered in the vicinity of $x = 0$ and, despite the model being able to generate accurate results even at such situations, its convergence rate might decay leading to an increased number of points being necessary to retrieve an accurate solution. Further discussion is provided in Subsec. III B.

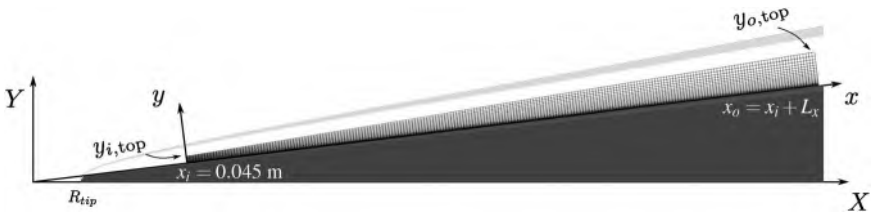

FIG. 1. Computational grid arrangement, which is refined in the wall normal direction to better resolve the boundary layer. Sharp ($R_{tip} = 0$) and blunt ($R_{tip} = 2.5$ mm) geometries were simulated.

A. Linearized Navier–Stokes equations

The governing equations for a compressible ideal gas are the continuity equation, the conservation of momentum in the three spatial directions, the conservation of energy, and the equation of state. These are written, respectively, as follows:

$$\frac{\partial \rho}{\partial t} + \nabla(\rho \mathbf{u}) = 0, \tag{4a}$$

$$\rho\left[\frac{\partial \mathbf{u}}{\partial t} + (\mathbf{u}\cdot\nabla)\mathbf{u}\right] = -\nabla P + \nabla\cdot[\lambda(\nabla\cdot\mathbf{u})\mathbf{I}] + \nabla\cdot\left[\mu(\nabla\mathbf{u} + \nabla\mathbf{u}^T)\right], \tag{4b}$$

$$\rho c_p\left[\frac{\partial T}{\partial t} + (\mathbf{u}\cdot\nabla)T\right] = \nabla\cdot(k\nabla T) + \frac{\partial P}{\partial t} + (\mathbf{u}\cdot\nabla)P + \Phi, \tag{4c}$$

$$\Phi = \lambda(\nabla\cdot\mathbf{u})^2 + 2\mu\left[\left(\frac{\partial u}{\partial x}\right)^2 + \left(\frac{\partial v}{\partial y}\right)^2 + \left(\frac{\partial w}{\partial z}\right)^2\right] + \mu\left[\left(\frac{\partial v}{\partial x} + \frac{\partial u}{\partial y}\right)^2 + \left(\frac{\partial w}{\partial x} + \frac{\partial u}{\partial z}\right)^2 + \left(\frac{\partial w}{\partial y} + \frac{\partial v}{\partial z}\right)^2\right], \tag{4d}$$

$$P = \rho R T. \tag{4e}$$

The linearized governing equations are then obtained by assuming the existence of a steady base flow that must also be a solution of the governing equations themselves. Moreover, the following derivation assumes that the perturbations are two dimensional and that the boundary layer grows spatially slowly (parallel flow assumption). A summary of additional considerations made is provided hereafter,

$$u = \bar{U} + \tilde{u}, \quad v = \tilde{v}, \quad w = 0, \quad P = \tilde{p}, \quad \rho = \bar{\rho} + \tilde{\rho}, \tag{5}$$

$$T = \bar{T} + \tilde{T}, \quad \mu = \bar{\mu} + \tilde{\mu}, \quad \lambda = \bar{\lambda} + \tilde{\lambda}, \quad k = \bar{k} + \tilde{k}, \tag{6}$$

where the total quantities are related to their respective base ($^-$) and perturbation ($\tilde{}$) fields.

The final set of linearized governing equations is obtained when the aforementioned set of considerations is applied and it is written in the following, where the overbar notation for the base state quantities was dropped for clarity:

$$\frac{\partial \tilde{\rho}}{\partial t} + U\frac{\partial \tilde{\rho}}{\partial x} + \rho\frac{\partial \tilde{u}}{\partial x} + \rho\frac{\partial \tilde{v}}{\partial y} + \frac{\partial \rho}{\partial y}\tilde{v} = 0, \tag{7a}$$

$$\rho\left[\frac{\partial \tilde{u}}{\partial t} + U\frac{\partial \tilde{u}}{\partial x} + \tilde{v}\frac{\partial U}{\partial y}\right] = -\frac{\partial \tilde{p}}{\partial x} + \frac{\partial}{\partial x}\left\{2\mu\frac{\partial \tilde{u}}{\partial x} + \lambda(\nabla\cdot\tilde{\mathbf{u}})\right\} + \frac{\partial}{\partial y}\left\{\mu\left[\frac{\partial \tilde{v}}{\partial x} + \frac{\partial \tilde{u}}{\partial y}\right] + \tilde{\mu}\frac{\partial U}{\partial y}\right\}, \tag{7b}$$

$$\rho\left[\frac{\partial \tilde{v}}{\partial t} + U\frac{\partial \tilde{v}}{\partial x}\right] = -\frac{\partial \tilde{p}}{\partial y} + \frac{\partial}{\partial x}\left\{\mu\left[\frac{\partial \tilde{v}}{\partial x} + \frac{\partial \tilde{u}}{\partial y}\right] + \tilde{\mu}\frac{\partial U}{\partial y}\right\} + \frac{\partial}{\partial y}\left\{2\mu\frac{\partial \tilde{v}}{\partial y} + \lambda(\nabla\cdot\tilde{\mathbf{u}})\right\}, \tag{7c}$$

$$\rho c_p\left[\frac{\partial \tilde{T}}{\partial t} + U\frac{\partial \tilde{T}}{\partial x} + \tilde{v}\frac{\partial T}{\partial y}\right] = \frac{\partial \tilde{p}}{\partial t} + U\frac{\partial \tilde{p}}{\partial x} + \frac{\partial}{\partial x}\left[k\frac{\partial \tilde{T}}{\partial x}\right] + \frac{\partial}{\partial y}\left[k\frac{\partial \tilde{T}}{\partial y} + \tilde{k}\frac{\partial T}{\partial y}\right] + \tilde{\Phi}, \tag{7d}$$

$$\tilde{\Phi} = 2\mu\frac{\partial U}{\partial y}\left(\frac{\partial \tilde{u}}{\partial y} + \frac{\partial \tilde{v}}{\partial x}\right) + \tilde{\mu}\left(\frac{\partial U}{\partial y}\right)^2, \tag{7e}$$

$$\tilde{\rho} = \frac{\tilde{p}}{RT} - \frac{\rho\tilde{T}}{T}. \tag{7f}$$

To make this system of equations simpler to solve some further steps must be taken. First, one can relate the conductivity (k) and the second viscosity coefficient (λ) to the molecular viscosity (μ) as

$$k = \frac{\mu c_p}{Pr}, \quad \lambda = -\frac{2}{3}\mu. \tag{8}$$

In addition, the viscosity perturbation can be represented as a function of temperature and its perturbation as follows:

$$\tilde{\mu} = \frac{\partial \mu}{\partial T}\tilde{T}. \tag{9}$$

Furthermore, one can use the fact that the base pressure is uniform through the boundary layer to remove the base density of the system of equations with the help of the equation of state

$$\rho = \frac{\rho_e T_e}{T}. \tag{10}$$

Ultimately, the following ansatz is made about the perturbations:

$$\tilde{f} = \hat{f}(y)e^{\kappa x - j\omega t}, \tag{11}$$

which are assumed to be waves traveling in the streamwise direction with a modal shape dependent on the wall normal coordinate and where κ and ω are the complex wavenumber and frequency, respectively. With all these assumptions, the linearized Navier–Stokes reduce to the following set of equations:

$$-j\omega\left[\frac{1}{RT}\hat{p} - \frac{\rho_e T_e}{T^2}\hat{T}\right] = -U\left[\frac{1}{RT}\kappa\hat{p} - \frac{\rho_e T_e}{T^2}\kappa\hat{T}\right] - \frac{\rho_e T_e}{T}\left[\kappa\hat{u} + \frac{\partial \hat{v}}{\partial y}\right] + \frac{\rho_e T_e}{T^2}\frac{\partial T}{\partial y}\hat{v}, \tag{12a}$$

$$\frac{\rho_e T_e}{T}\left[-j\omega\hat{u} + U\kappa\hat{u} + \hat{v}\frac{\partial U}{\partial y}\right] = -\kappa\hat{p} + \frac{4}{3}\mu\kappa^2\hat{u} + \frac{1}{3}\mu\kappa\frac{\partial \hat{v}}{\partial y} + \frac{\partial}{\partial y}\left\{\frac{\partial \mu}{\partial T}\hat{T}\frac{\partial U}{\partial y}\right\} + \frac{\partial \mu}{\partial y}\left[\kappa\hat{v} + \frac{\partial \hat{u}}{\partial y}\right], \tag{12b}$$

$$\frac{\rho_e T_e}{T}[-j\omega\hat{v} + U\kappa\hat{v}] = -\frac{\partial \hat{p}}{\partial y} + \mu\kappa^2\hat{v} + \frac{4}{3}\mu\frac{\partial^2 \hat{v}}{\partial y^2} + \frac{1}{3}\mu\kappa\frac{\partial \hat{u}}{\partial y} + \frac{\partial \mu}{\partial T}\frac{\partial U}{\partial y}\kappa\hat{T} + 2\frac{\partial \mu}{\partial y}\left[\frac{2}{3}\frac{\partial \hat{v}}{\partial y} - \frac{1}{3}\kappa\hat{u}\right], \tag{12c}$$

$$\frac{\rho_e T_e}{T}\left[-j\omega\hat{T} + U\kappa\hat{T} + \hat{v}\frac{\partial T}{\partial y}\right] = \frac{1}{c_p}(-j\omega\hat{p} + U\kappa\hat{p}) + \frac{\mu}{Pr}\left(\kappa^2\hat{T} + \frac{\partial^2 \hat{T}}{\partial y^2}\right) + \frac{1}{Pr}\frac{\partial}{\partial y}\left(\frac{\partial \mu}{\partial T}\hat{T}\frac{\partial T}{\partial y}\right) + \frac{\partial}{\partial y}\left[\frac{\mu}{Pr}\right]\frac{\partial \hat{T}}{\partial y} + 2\frac{\mu}{c_p}\frac{\partial U}{\partial y}\left(\frac{\partial \hat{u}}{\partial y} + \kappa\hat{v}\right) + \frac{1}{c_p}\frac{\partial \mu}{\partial T}\hat{T}\left(\frac{\partial U}{\partial y}\right)^2. \tag{12d}$$

B. Laguerre–Galerkin discretization

The system of Eqs. (12) can be written as an operator ($\mathscr{R}$), called the residue, acting on a perturbation vector, i.e., $\mathscr{R}\hat{f} = 0$. Moving forward, one can assume a polynomial expansion for the wall normal mode shapes,

$$\hat{f}(y) \approx \check{f}_N = \Sigma_{j=1}^{N} \check{f}_j \psi_j, \tag{13}$$

represented here as a sum of basis functions ψ_j weighted by the coefficients $\check{f}_j$.

Since this is only a finite approximation of the infinite expansion that constitutes the exact solution, the substitution of the aforementioned polynomial expansion into the linearized equations leads to a non-zero residual (ε_N). As the polynomial order (N) of the expansion increases and approaches infinity, the approximate solution tends to the exact one and the residual vanishes. Assuming a finite N though, the residual can be minimized by making it orthogonal to the N-dimensional subspace

$$\langle \varepsilon_N, \psi_i \rangle = \langle \mathscr{R}\hat{f}, \psi_i \rangle - \langle \mathscr{R}\check{f}_N, \psi_i \rangle = 0. \tag{14}$$

Ultimately, the values for $\check{f}_j$ are found by solving the inner product with the finite set of basis functions,

$$\Sigma_{j=1}^{N} \int_D \mathscr{R}(\check{f}_j \psi_j) \psi_i d\mathbf{x} = 0, \tag{15}$$

which is a linear system of equations with the weighting coefficients as unknowns, i.e., $A_{ij}\check{f}_j = 0$.

The numerical efficiency of the method is directly influenced by the choice of the expansion basis since its accuracy depends on the approximation properties of the expansion functions, i.e., their capability of matching the boundary conditions of the initial problem. For the linear stability eigenvalue problem of a boundary layer, one expects the mode gradients to be concentrated near the wall and to decay as the distance from the boundary increases. This prompted the choice of the Laguerre functions $[\hat{L}_k(y)]$, a set of orthogonal polynomials defined on the positive half of the real number axis $[0, \infty)$ that decay exponentially (Shen *et al.*, 2011).

Following the implementation of the Galerkin method using Laguerre functions developed by Shen (2000), an initial basis that satisfies the homogenous Dirichlet boundary condition at the wall $[\check{f}(0) = 0]$ and the boundary condition at infinity $[\lim_{y\to\infty} \check{f}(y) = 0]$ is achieved by algebraic manipulation

$$\hat{\phi}_k(y) = \hat{L}_k(y) - \hat{L}_{k+1}(y). \tag{16}$$

The resulting basis, shown in Fig. 2, is then augmented by one Laguerre mode $\{\psi_j(y)\} = \{\hat{L}_1(y), \hat{\phi}_1(y), \hat{\phi}_2(y), \ldots, \hat{\phi}_{j-1}(y)\}$. This introduces one function with a non-zero value at the boundary and makes it possible to lift the solution to any required non homogenous condition by adjusting its weight. If a homogenous Dirichlet boundary condition is needed for a certain variable, the corresponding weight for $\hat{L}_1$ should be set to zero.

The integrals described in Eq. (14) are evaluated using the Gauss–Radau–Laguerre quadrature, where the nodes and weights are obtained using a modified Jacobi matrix of order $N+1$, fully described in Gautschi (2002). The eigenvalues of such matrix coincide with the node locations and the weights can be expressed as function of the associated normalized eigenvectors.

One should note that, as the order of the Gauss–Radau–Laguerre quadrature grows, the location of its nodes move away from $y = 0$ to better capture the asymptotic behavior at infinity. This results in the unwanted shift of the majority of the quadrature nodes outside the region of interest for the problem. To overcome this difficulty, a length scale ($y_{\max}$) related to the distance where an *effective infinity* would have already been reached is used to normalize the basis functions so that all the quadrature points are located in the associated region of interest, i.e., below $y_{\max}$. Such scaling of the Gauss–Radau–Laguerre quadrature collocation points was shown by Shen (2000) to lead to higher numerical accuracy.

The effect of the aforementioned scaling is shown in Fig. 2, where the first six modes of the basis $\phi_k(y)$ and $\hat{L}_1$ are plotted for two polynomial orders, $N = 32$ and $N = 64$. When the order of the polynomial expansion

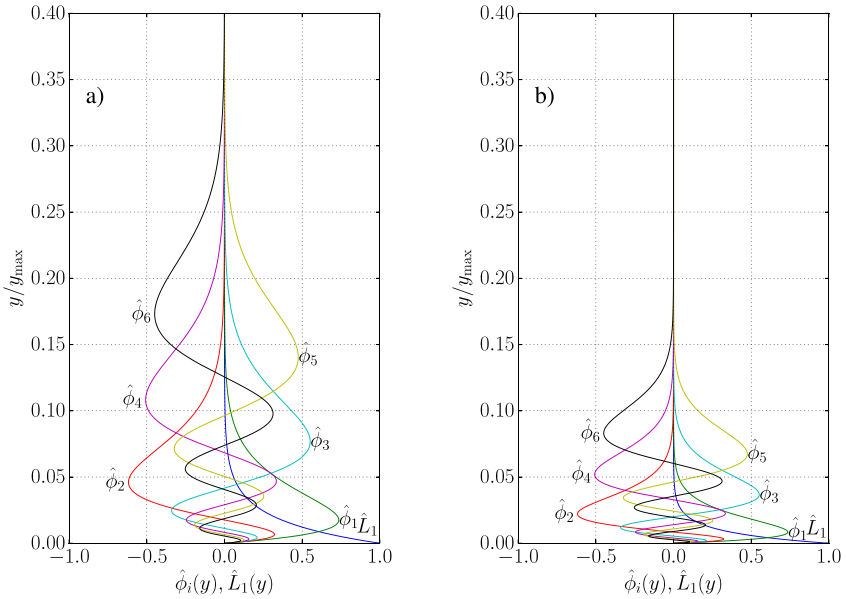

FIG. 2. Mode shapes of the first six components of $\hat{\phi}_k(y)$ and $\hat{L}_1(y)$ for polynomial expansions of order 32 (a) and 64 (b). In order to increase the accuracy of numerical procedure, the Laguerre functions are scaled into a region of interest.

is increased and the size of the region of interest remains the same, the scaling effect concentrates modal gradients close to the boundary.

The previously derived linearized Navier–Stokes equations can be expanded based on the $\psi_j(y)$ basis functions and the residual of such operation can be minimized resulting in a linear system of equations as in 14. The resulting system have the mode shapes of pressure ($\check{\mathbf{p}}$), streamwise ($\check{\mathbf{u}}$) and wall normal ($\check{\mathbf{v}}$) velocity components, and temperature ($\check{\mathbf{T}}$) as unknowns which are operated on by the following matrices:

$$\mathbf{M}[g] = \int_D g\psi_i\psi_j d\mathbf{x}, \quad \mathbf{C}_y[g] = \int_D g\psi_i \frac{\partial\psi_j}{\partial y} d\mathbf{x}, \quad \mathbf{C}_{y^2}[g] = \int_D g\psi_i \frac{\partial^2\psi_j}{\partial y^2} d\mathbf{x}, \tag{17}$$

dependent only on the basis functions. The components of such matrices are numerically obtained by evaluating the integrals thorough the Gauss–Radau–Laguerre quadrature. Ultimately, a generalized eigenvalue problem is reached and its representation as a system of matrix equations is shown as follows:

$$\omega\left(\mathbf{M}\left[\frac{1}{RT}\right]\cdot\check{\mathbf{p}} - \mathbf{M}\left[\frac{\rho_e T_e}{T^2}\right]\cdot\check{\mathbf{T}}\right) + \kappa\left(\mathbf{M}\left[\frac{U}{RT}\right]\cdot\check{\mathbf{p}} - \mathbf{M}\left[\frac{U\rho_e T_e}{T^2}\right]\cdot\check{\mathbf{T}} + \mathbf{M}\left[\frac{\rho_e T_e}{T}\right]\cdot\check{\mathbf{u}}\right) + \mathbf{C}_y\left[\frac{\rho_e T_e}{T}\right]\cdot\check{\mathbf{v}} - \mathbf{M}\left[\frac{\rho_e T_e}{T^2}\frac{\partial T}{\partial y}\right]\cdot\check{\mathbf{v}} = 0, \tag{18a}$$

$$\omega\left(\mathbf{M}\left[\frac{\rho_e T_e}{T}\right]\cdot\check{\mathbf{u}}\right) + \kappa\left(\mathbf{M}\left[\frac{\rho_e T_e U}{T}\right]\cdot\check{\mathbf{u}} + \mathbf{M}\cdot\check{\mathbf{p}}\right. \left. t - \frac{4}{3}\mathbf{M}[\mu]\cdot\kappa\check{\mathbf{u}} - \frac{1}{3}\mathbf{C}_y[\mu]\cdot\check{\mathbf{v}} - \mathbf{M}\left[\frac{\partial\mu}{\partial y}\right]\cdot\check{\mathbf{v}}\right) + \mathbf{M}\left[\frac{\rho_e T_e}{T}\frac{\partial U}{\partial y}\right]\cdot\check{\mathbf{v}} - \mathbf{M}\left[\frac{\partial}{\partial y}\left(\frac{\partial\mu}{\partial T}\frac{\partial U}{\partial y}\right)\right]\cdot\check{\mathbf{T}} - \mathbf{C}_y\left[\frac{\partial\mu}{\partial T}\frac{\partial U}{\partial y}\right]\cdot\check{\mathbf{T}} - \mathbf{C}_y\left[\frac{\partial\mu}{\partial y}\right]\cdot\check{\mathbf{u}} = 0, \tag{18b}$$

$$\omega\left(\mathbf{M}\left[\frac{\rho_e T_e}{T}\right]\cdot\check{\mathbf{v}}\right) + \kappa\left(\mathbf{M}\left[\frac{\rho_e T_e U}{T}\right]\cdot\check{\mathbf{v}} - \frac{1}{3}\mathbf{C}_y[\mu]\cdot\check{\mathbf{u}} - \mathbf{M}[\mu]\cdot\kappa\check{\mathbf{v}} - \mathbf{M}\left[\frac{\partial\mu}{\partial T}\frac{\partial U}{\partial y}\right]\cdot\check{\mathbf{T}} + \frac{2}{3}\mathbf{M}\left[\frac{\partial\mu}{\partial y}\right]\cdot\check{\mathbf{u}}\right) + \mathbf{C}_y\cdot\check{\mathbf{p}} - \frac{4}{3}\mathbf{C}_{y^2}[\mu]\cdot\check{\mathbf{v}} - \frac{4}{3}\mathbf{C}_y\left[\frac{\partial\mu}{\partial y}\right]\cdot\check{\mathbf{v}} = 0, \tag{18c}$$

$$\omega\left(\mathbf{M}\left[\frac{\rho_e T_e}{T}\right]\cdot\check{\mathbf{T}} - \frac{1}{c_p}\mathbf{M}\cdot\check{\mathbf{p}}\right) + \kappa\left(\mathbf{M}\left[\frac{\rho_e T_e U}{T}\right]\cdot\check{\mathbf{T}} - \frac{1}{c_p}\mathbf{M}[U]\cdot\check{\mathbf{p}} - \mathbf{M}\left[\frac{\mu}{Pr}\right]\cdot\kappa\check{\mathbf{T}} - 2\mathbf{M}\left[\frac{\mu}{c_p}\frac{\partial U}{\partial y}\right]\cdot\check{\mathbf{v}}\right) + \mathbf{M}\left[\frac{\partial T}{\partial y}\frac{\rho_e T_e}{T}\right]\cdot\check{\mathbf{v}} - \mathbf{C}_{y^2}\left[\frac{\mu}{Pr}\right]\cdot\check{\mathbf{T}} - \mathbf{M}\left[\frac{1}{Pr}\frac{\partial}{\partial y}\left(\frac{\partial\mu}{\partial T}\frac{\partial T}{\partial y}\right)\right]\cdot\check{\mathbf{T}} - \mathbf{C}_y\left[\frac{1}{Pr}\frac{\partial\mu}{\partial T}\frac{\partial T}{\partial y}\right]\cdot\check{\mathbf{T}} - \mathbf{C}_y\left[\frac{\partial}{\partial y}\left(\frac{\mu}{Pr}\right)\right]\cdot\check{\mathbf{T}} - 2\mathbf{C}_y\left[\frac{\mu}{c_p}\frac{\partial U}{\partial y}\right]\cdot\check{\mathbf{u}} - \mathbf{M}\left[\frac{1}{c_p}\frac{\partial\mu}{\partial T}\left(\frac{\partial U}{\partial y}\right)^2\right]\cdot\check{\mathbf{T}} = 0. \tag{18d}$$

In possession of Eqs. (4) one can chose to solve a temporal or a spatial stability problem. To solve the time dependent problem, one should specify an imaginary wavenumber (κ) and solve for the complex frequency (ω) as

$$(\mathscr{K} + \omega\mathscr{M})\hat{\mathbf{u}} = 0, \tag{19}$$

where $\hat{\mathbf{u}} = (\check{\mathbf{p}}, \check{\mathbf{u}}, \check{\mathbf{v}}, \check{\mathbf{T}})$. The equivalent spatial stability problem requires first that one linearizes the equations by solving for $\tilde{\mathbf{u}} = (\check{\mathbf{p}}, \check{\mathbf{u}}, \check{\mathbf{v}}, \check{\mathbf{T}}, \kappa\check{\mathbf{u}}, \kappa\check{\mathbf{v}}, \kappa\check{\mathbf{T}})$. After this step is done, one specifies a real frequency (ω) and solve for the complex wavenumber (κ) as

$$(\tilde{\mathscr{K}} + \kappa\tilde{\mathscr{M}})\tilde{\mathbf{u}} = 0. \tag{20}$$

C. LST verification

The described method for solving the linear stability equations was compared against previously published results for the temporal stability of compressible boundary layers by Malik *et al.* (1990) and Chen *et al.* (2017) (see Table III), showing good agreement. For the adiabatic wall $M = 10$ boundary layer case, the current work predicts a slightly smaller temporal growth rate in comparison with the previously published results. Since the mode's amplitude peak moves away from the wall in this case, it is assumed that the necessity of including an unphysical boundary condition at the top of the computational domain might exert more influence in comparison to the isothermal wall cases. If that assumption is correct, the use of the Laguerre functions and its property of exponential decay are expected to be more accurate since it naturally satisfies the physical boundary conditions. More evidence is necessary before this claim is confirm though. Results here are normalized with respect to the length scale $\ell_e = \sqrt{\nu_e x/u_e}$, where the subscript e is used to indicate that the values are at the edge of the boundary layer. R is the Reynolds number related to ℓ_e and it can be shown that $xRe_m = R^2$ and κ is the wavenumber associated with the modal expansion (11).

IV. HYPERSONIC BOUNDARY LAYER INSTABILITY ATTENUATION VIA POROUS CARBON-MATRIX CERAMICS

A. Analysis of the experimental conditions reported by Wagner *et al.* (2013)

This subsection analyzes the evolution of small disturbances in an axisymmetric hypersonic flow setup over impermeable and porous walls modeled via the TDIBC (Scalo *et al.*, 2015) which are compared against results obtained from the spectral LST solver presented in Sec. III. A sharp cone and a blunt cone with 2.5 mm nose-tip radius were considered as per the experimental setup described in Wagner *et al.* (2013). The initial conditions of the laminar base state for the sharp cone were obtained by blending the Blasius solution for a zero pressure gradient axisymmetric boundary layer with the inviscid Taylor–Maccoll solution for the inviscid flow field. The base flow of the blunt cone was provided by a low-order precursor simulation performed using the DLR FLOWer code (Kroll and Fassbender, 2006). A more detailed description of these calculations can be found in Wartemann *et al.* (2014).

The simulations presented in the current section also serve the purpose of assessing the ability of the quasi-spectral viscosity (QSV) approach (Sousa and Scalo, 2022) to deactivate itself in the absence of

TABLE III. Comparison of current LST results against previous literature.

M	T_0 (°R)	$\frac{T_w}{T_{adb}}$	R	κ	Malik (1990)	Chen *et al.* (2017)	Current work
0.5	500	1.0	2000	0.1	$0.029\,08 + 0.002\,244i$	$0.029\,09 + 0.002\,244i$	$0.029\,11 + 0.002\,244i$
10	4200	0.1	2000	0.105	$0.097\,48 + 0.002\,030i$	⋯	$0.097\,43 + 0.002\,068i$
10	4200	1.0	1000	0.12	$0.115\,86 + 0.000\,153i$	$0.115\,86 + 0.000\,147i$	$0.115\,86 + 0.000\,137i$

turbulence, hence being able to correctly capture pure second-mode wave linear dynamics. While QSV closure is not required for the current axisymmetric runs, it is necessary to numerically stabilize three-dimensional transitional simulations at the same conditions, which suffer from harsh grid requirements dictated by the strong wall-cooling conditions ($T_w/T_{adb} \approx 0.08$) and the viscous constraints from the buffer-layer turbulence forming after transition.

A transient adjustment of the numerical solution on the computational grid is first observed after the initialization of the simulations for all Re_m and nose tip radii considered. All simulations are carried out until a steady state is reached, resulting in the profiles shown in Figs. 3 and 4, plotted for various streamwise locations. A simulation is considered to have reached steady state conditions if temporal changes in the pressure field in time are less than 10^{-8} of the base pressure. For all cases considered, an excellent agreement between the Blasius or precursor results and the obtained quiet flow is observed. As the Reynolds numbers increases, the boundary layer thicknesses decreases. Additionally, the blunt tip induces an entropy layer that affects the near-wall profiles leading to a thicker boundary layer near the nose tip. However, as the flow develops downstream, the relative importance of the nose tip bluntness in the flow decreases and the profiles eventually converge to those predicted by the self-similar conical Blasius. This determines the existence of two regions: one near the tip, where the slightly blunted shock thickens the boundary layer, followed by a zone where the boundary layer grows in space slower than for the sharp cone.

Following the establishment of an unperturbed laminar state for all cases, a broadband pulse disturbance is introduced via a low amplitude ($a = 1$ m/s) suction and blowing at the wall, as shown in Fig. 5. The single-time pulse is imposed with a period of $1/f_p$, where $f_p = 600$ kHz. Because its signal is concentrated in the time-domain, its Fourier transform has a broadband characteristic. In fact, this is the same mathematical argument behind Heisenberg's uncertainty principle. More specifically, Fig. 10 of Sousa *et al.* (2019) shows the imposed broadband spectrum of such a perturbation in a region just downstream of the suction and blowing pulse with dotted lines and it illustrates that all the disturbances whose frequency content lie between 100 and 1100 kHz are excited within the same order of magnitude. Taking this into consideration, if one analyzes the unstable regions for sharp and blunt cones at $Re_m = 4.06 \times 10^6\ \mathrm{m}^{-1}$ shown in Fig. 7 and observes that the second-modal instability lies between 300 and 800 kHz within the region of interest for the present setup, it is possible to conclude that the introduced pulse disturbance is capable of exciting all the frequency range relevant for second-modal instabilities for this problem. The pulse is applied in a streamwise strip of $0.01\,L_x$ in length and centered around $x = 0.05$ m, via the following:

$$v(x, y = 0, t) = a\cos(\pi\xi)^3 \sin(2\pi f_p t), \quad \text{for } 0 \le t \le 1/f_p, \quad (21)$$

where ξ is a normalized variable with values in the $[-1, 1]$ range, which is mapped to the physical extent of the strip where the pulse is applied. This perturbation aims at mimicking a natural transition

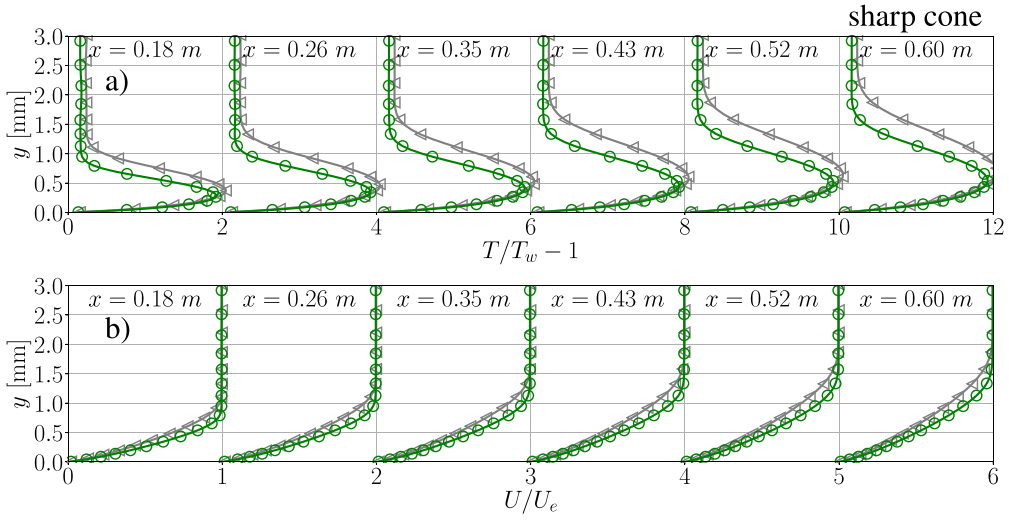

FIG. 3. Temperature (a) and streamwise velocity (b) profiles for sharp cone at $Re_m = 2.43 \times 10^6\ \mathrm{m}^{-1}$ (gray left triangle) and $Re_m = 4.06 \times 10^6\ \mathrm{m}^{-1}$ (green circle). Results from the unperturbed simulation (——) are compared against the similarity profile obtained from Mangler-transformed Blasius (Lees, 1956), shown in symbols (gray left triangle; green circle). Color coding is consistent with Table I.

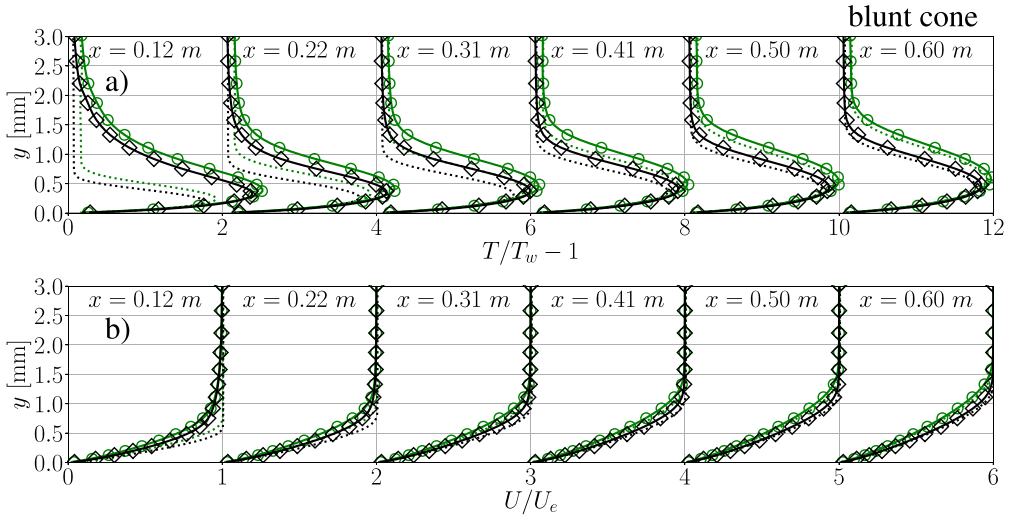

FIG. 4. Temperature (a) and streamwise velocity (b) profiles for a 2.5 mm-tip cone at $Re_m = 4.06 \times 10^6\ m^{-1}$ (green circle) and $Re_m = 6.40 \times 10^6\ m^{-1}$ (black diamond). Results from the unperturbed simulation (——) are compared against the similarity profile obtained from Mangler-transformed Blasius solution for a sharp cone (·····) and the solution from the DLR FLOWer precursor simulation (green circle; black diamond). Color coding is consistent with Table I.

scenario due to its broadband characteristics. It was first used by Gaster and Grant (1975) in incompressible transition simulations and by Sivasubramanian and Fasel (2014) to study its high speed counterpart. The same strategy was used by Sousa *et al.* (2019) demonstrating second-mode attenuation by an impedance boundary condition modeling the same C/C material considered in the present work but only on a sharp cone. Although this approach introduces a nonzero net mass flux due to the nonzero correlation between velocity and density fluctuations at the wall, the maximum density fluctuation amplitude is only on the order of 0.3% when compared to the base density, ρ_0.

The current manuscript extends the previous work by the same authors to include the effect on nose tip bluntness with new companion LST results. Porous walls are modeled with an impedance boundary condition introduced in the Navier–Stokes solver as a TDIBC and in the LST solver directly in the frequency domain, as obtained by fitting the ultrasonic experimental benchtest measurements (see Sec. 2 of the Appendix).

To ensure that the evolution of the high-frequency perturbations is accurately captured, a grid sensitivity study is performed over impermeable walls for the both Reynolds numbers considered and for each nose tip configuration. Results for the amplitude of the wall pressure perturbations are shown for a progression of grid resolutions in Fig. 6. The second-mode amplitude is slightly under predicted on the coarser grid ($n_x = 2048$, $n_y = 96$) for the sharp-nosed cone at $Re_m = 2.40 \times 10^6\ m^{-1}$ but, apart from that, all the other cases qualitatively converge.

By comparing the results of the second-mode amplitude evolution for the sharp and blunt cases, it is seen that a much wider range of unstable frequencies is present over a sharp cone. The reason behind this effect is twofold: first, the entropy layer's stabilizing effect reduces the region of second-mode growth over the 2.5 mm blunt cone and the high-frequency unstable region typically observable over a sharp cone disappears; second, the presence of the nose tip bluntness shifts the unstable frequency band to lower frequencies after the swallowing of the entropy layer (Fig. 7). The shift is bigger around $X = 0.3$ m and it decreases as the distance from the nose tip increases. Due to the relation between the boundary layer thickness and the second-mode frequency band (Stetson, 1990), one can explain this behavior by observing the boundary layer profiles shown in Fig. 4. As the profiles evolve downstream, the influence of the blunt tip diminishes and, eventually, the boundary layer thickness follows, a self-similar profile. This means that the blunt cone boundary layer thickness changes less rapidly than the corresponding one over a sharp cone, which ultimately concentrates the region of second-mode instability in a narrower frequency band.

Softley (1969) observed that, up to a nose-tip-radius Reynolds number ($Re_{\text{nose}} = R_{\text{tip}} Re_m$) of approximately 10^5, the bluntness is

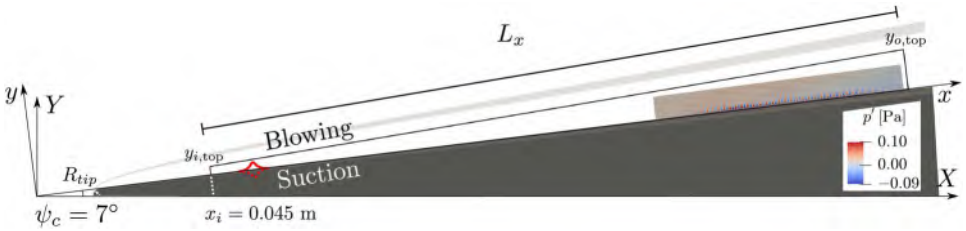

FIG. 5. Schematic representation of broadband disturbance excitation through a one-time suction and blowing pulse at the wall. Sharp ($R_{tip} = 0$) and blunt ($R_{tip} = 2.5$ mm) geometries were simulated.

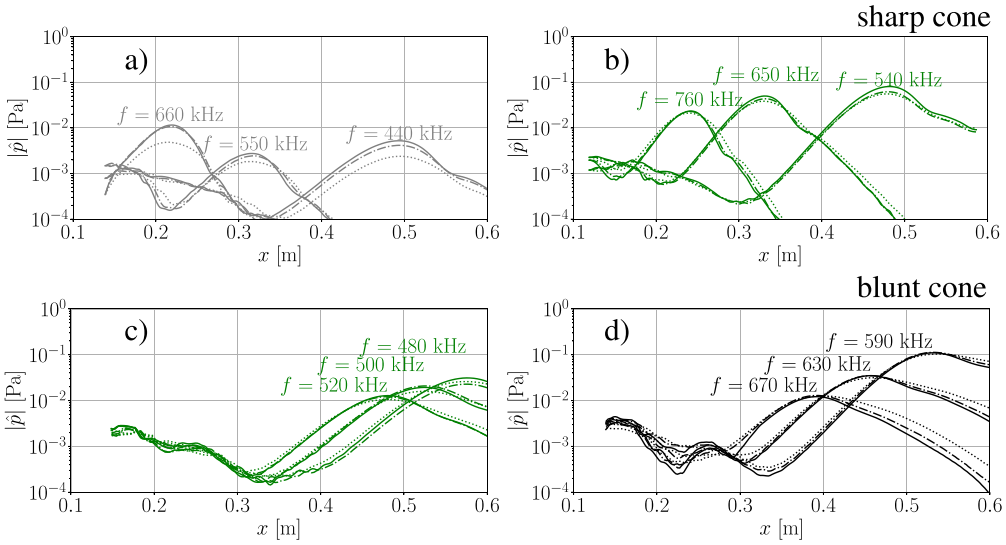

FIG. 6. Grid sensitivity analysis for various frequency components of the wall pressure perturbation amplitude in an axisymmetric simulation of broadband pulse propagation. Results are shown for grid sizes: $n_x \times n_y = 2048 \times 96$ (·····); $n_x \times n_y = 3072 \times 144$ (– · – · – · –); and $n_x \times n_y = 4608 \times 192$ (——). Flow conditions are for Reynolds numbers: (a) $Re_m = 2.43 \times 10^6$ m^{-1} in gray; (b) and (c) $Re_m = 4.06 \cdot 10^6$ m^{-1} in green; and (d) $Re_m = 6.40 \times 10^6$ m^{-1} in black. See Table I for the complete color scheme.

considered small and it delays transition. This trend is reversed after $Re_{\text{nose}} \geq 10^5$, with bluntness promoting transition. At the flow conditions and cone geometries studied in the current work, the largest Re_{nose} value is around 1.6×10^4; therefore, the stabilizing effect caused by bluntness observed in Fig. 6 is in agreement with previous literature.

The effects of surface boundary conditions on the evolution of a given Fourier component of the pulse disturbance are analyzed in Fig. 8 via the instantaneous wall pressure distribution for different frequencies, Reynolds numbers and nose tip bluntness. Figure 8 shows that the amplitude of the surface pressure oscillations are comparable between impermeable and porous cases in the region before $x \simeq 0.19$ m ($X = 0.182$ m), where the porous insert starts, for any given Re_m and tip geometry. As the pulse evolves over the impedance boundary, acoustic energy is removed from the disturbance. The overall second-mode attenuation is achieved not only by decreasing the growth rates in the regions of instability but also by increasing the attenuation rates in the region where it is stable. The combination of both effects leads to the amplitude of the surface pressure oscillation signal over a porous surface to be always lower than over the impermeable surface.

Additionally, Fig. 8 shows that an increase in the Re_m leads to a higher potential for wave attenuation for a given nose geometry. This is connected to the increase in the acoustic absorption coefficient (β) with static pressure (see Fig. 14), which is, in turn, directly proportional to the freestream Re_m connected to the experimental conditions (Table I).

Furthermore, these results are compared against a novel in-house linear stability theory (LST) solver based on a Legendre spectral approximation (see the Appendix). Since the LST solver only returns spatial growth rate information and mode shapes without an absolute amplitude, a choice is made in the current work to show the amplitude of the signal reconstructed via backward integration starting from the second neutral point observed in the axisymmetric calculations. This choice avoids the numerical evaluation of the spatial derivative of the wall pressure disturbance amplitude near the first neutral point, which is made noisy by the low amplitude values and can even be below the numerical noise ($\simeq 10^{-8} p_\infty$) existent in the simulations, as is the case for the flow over the blunt-nosed geometries considered (Fig. 8).

Results from the high-order calculations for all cases considered follow closely the LST predictions. Small discrepancies are observed

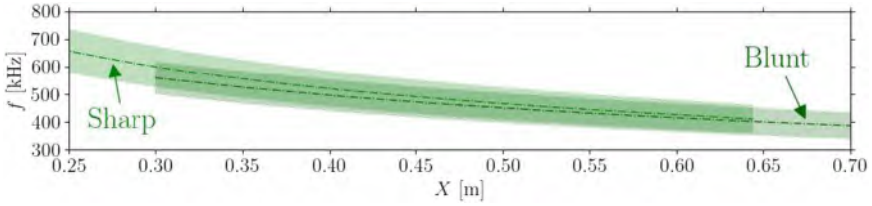

FIG. 7. LST predictions for the second-mode instability regions over both a sharp- and a blunt-nosed cone at flow conditions related to the HEG experimental conditions at $Re_m = 4.06 \times 10^6$ m^{-1} (Table I). The dash-dotted line represents the location of maximum growth and the region between the first and second neutral growth rate points is shaded.

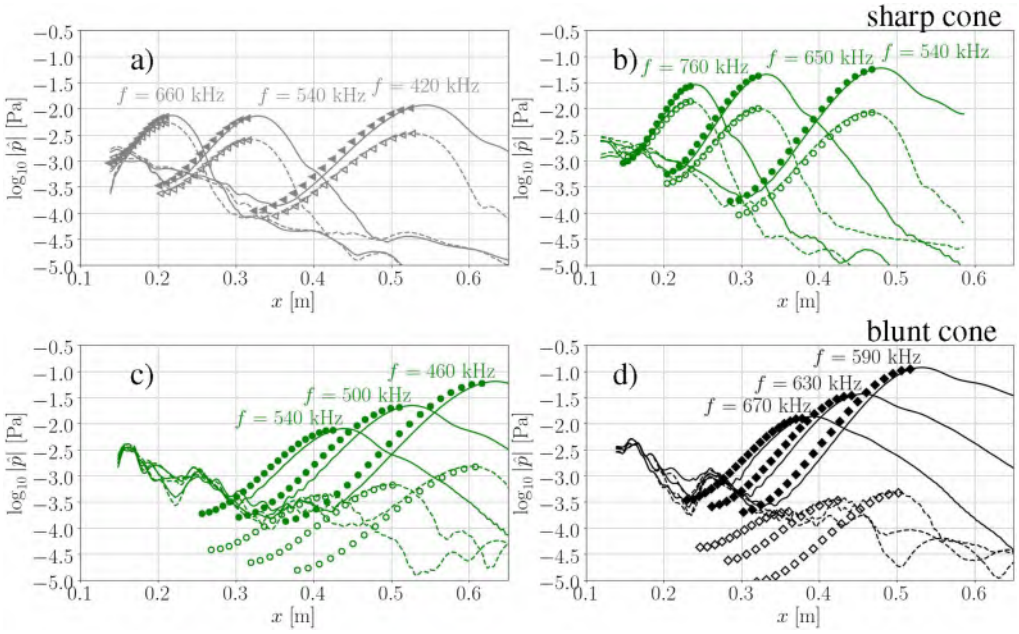

FIG. 8. Comparison between axisymmetric simulations, with QSV closure active (lines), and LST (symbols) predictions for various Fourier components of wall pressure fluctuations as a function of space. Impermeable walls: —— and (gray filled left triangle, green filled circle, black filled diamond); porous walls: – – – and (gray left triangle, green circle, black diamond). Flow conditions are for Reynolds numbers: (a) $Re_m = 2.43 \times 10^6$ m^{-1} in gray; (b) and (c) $Re_m = 4.06 \times 10^6$ m^{-1} in green; (d) $Re_m = 6.40 \times 10^6$ m^{-1} in black. See Table I for the complete color and symbol scheme.

especially for the impermeable wall blunt-nosed case for both Reynolds numbers. The main reason for their occurrence is a mismatch between the LST-predicted location for the second neutral point. The magnitude of the predicted and recovered growth rates, though, are in agreement since a slight shift of the curves is sufficient to collapse the curves. The small discrepancies that are observed are attributed to both nonlinear effects and deviations from the parallel flow assumption used in the derivation of the linear stability equations. The influence of secondary nonlinear effects is evidenced by the fact that the agreement between LST and pulsed simulations is improved when porous walls are considered for all cases: the attenuating effect of porous walls leads to smaller disturbances levels and decreased influence of nonlinear effects. Moreover, if all the individual Fourier modes of the wall pressure oscillation signal are plotted concomitantly, as in Fig. 9, an initial development of higher harmonics indicating the emergence of nonlinearities is observed. Even though the harmonics are more clearly observed in later portions of the streamwise extent of the domain, due to the presence of a noise floor, their development starts at earlier stages where nonlinear effects would be already influencing the growth rates. Similar plots for the $Re_m = [2.43, 4.06] \times 10^6$ m^{-1} conditions over a sharp cone geometry are included in Sousa *et al.* (2019) and are not repeated here for the sake of conciseness.

Although some nonlinear effects are present, we argue that it was necessary to introduce disturbances in the simulations with the chosen

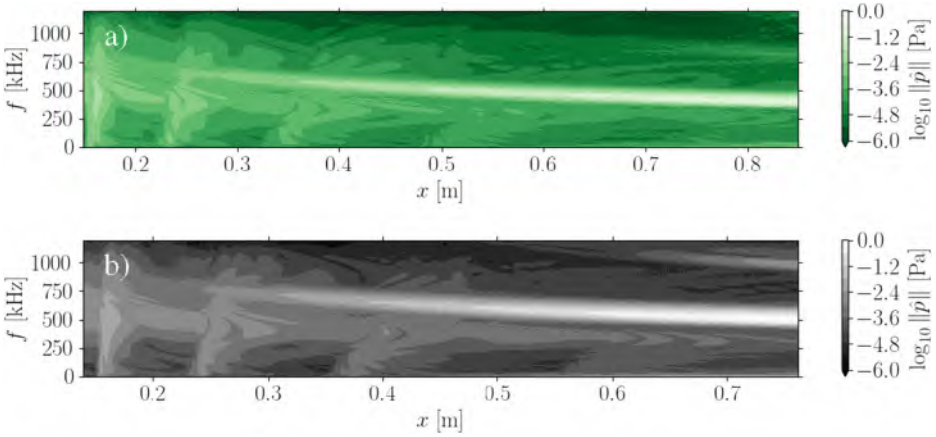

FIG. 9. Spatial evolution of the Fourier components of the surface pressure oscillations recovered from a broadband disturbance simulation over a blunt cone for (a) $Re_m = 4.06 \times 10^6$ m^{-1} in green and (b) $Re_m = 6.40 \times 10^6$ m^{-1} in black. See Table I for the complete color scheme.

amplitude level to allow the comparison between porous and impermeable walls as well as between different nose tips and flow conditions. In fact, it can be seen in Fig. 8 that the recovered signal over porous walls when a blunt-nosed geometry is considered is barely above the inherent noise floor level of the calculations.

Comparing the results obtained from the numerical simulations of the advection of a broadband disturbance with the ones predicted by linear stability theory, one can reach two conclusions: first, that the implementation of the TDIBC technique in the Navier–Stokes solver is numerically consistent between different solvers, and second, that the use of the QSV technique does not hinder the capability of accurately simulating the second-mode's instability dynamics. To the authors' knowledge, this is the first time that a dynamic large-eddy simulation technique has been demonstrated to preserve acoustic transitional waves in a hypersonic boundary layer.

B. Analysis of the experimental conditions reported by Willems *et al.* (2017)

Willems *et al.* (2017) performed hypersonic boundary layer transition experiments using a sharp 3° half angle cone in the BAM6QT quiet wind tunnel and the conventional H2K wind tunnel. The conditions under which the experiments were conducted are reported in Table IV. Porous surfaces formed by either regular drilled micro-holes or the C/C random porous structure were employed in the experiments and the collected data showed neither a damping of the second-mode nor a delay of the transition process.

In Sousa *et al.* (2019), the authors had speculated that the reason why the experiments conducted by Willems *et al.* (2017) were not able to measure any attenuation of the second-mode waves when advecting over a similar C/C-based surface as the one used in experiments by Wagner *et al.* (2013) is that the frequency of the second-mode waves were low (around 120 kHz) at the flow conditions chosen for that study (Table IV). This supposition is based on the fact that the acoustic absorption capability of the C/C surface rapidly deteriorates in the low frequency and low surface pressure region. The decreased attenuation performance of the C/C surface in low pressure environments was also noted by Wagner *et al.* (2015) while analyzing the application of such a material in hypersonic flight missions. Specifically, it was noted that the mission requirements of the *SKYLON* spaceplane lead to flow conditions that rendered an ultrasonic absorbing coating ineffective.

In order to confirm this hypothesis, it suffices to look into the experimental conditions tested under which the porous walls would be highest absorbing and, if little benefit is found under these conditions, all the other ones would also be expected to lead to similar results. The flow conditions at $Re_m = 9.5 \times 10^6\ \mathrm{m}^{-1}$ were chosen as an example since they had the highest freestream pressure which power spectrum measurements (Willems *et al.*, 2017) did not show signs of nonlinear energy flowing to higher harmonics up to $x = 0.80$ m. Experimental conditions with lower levels of freestream pressure are connected to lower base pressures at the surface and ultimately lead to lower acoustic absorption capabilities (see Figs. 11 and 14).

The Taylor–Maccoll ordinary differential equation (ODE) was used to recover the conical shock angle for a sharp cone with 3° half angle at the aforementioned operating conditions. Then, oblique shock relations were used to recover the surface pressure value of $P_w = 725$ Pa. If the homogeneous absorber theory (HAT) with the parameters fitted to the C/C acoustic response is used at such conditions, the corresponding absorption coefficient of $\beta = 0.026$ is achieved for the frequency of 120 kHz, measured in the experiments. This is much lower than the $\beta = 0.137$ expected for the frequency band around 380 kHz, which would be unstable at the same streamwise distance from the sharp cone tip for a 7° half angle at the HEG wind tunnel experimental conditions associate with $Re_m = 4.0 \times 10^6$ (Table I), for example. If the experiments by Willems *et al.* (2017) were performed over a 7° half angle cone, the pressure at the wall would increase to $P_w \approx 1153$ Pa and, in addition, the unstable frequency at a similar streamwise distance from the cone's tip would increase to ≈ 150 kHz. Both of these changes contribute to increasing the absorption coefficient of the C/C to $\beta \approx 0.039$, still much lower than in at conditions associated with experiments by Wagner *et al.* (2013).

The LST solver was used to predict the growth rate of the unstable frequencies for both experimental conditions using impermeable and porous surfaces as boundary conditions and the results are shown in Fig. 10. In the left plot, the results for the second-mode growth attenuation for Wagner *et al.* (2013) experimental conditions at $Re_m = 4.0 \times 10^6\ \mathrm{m}^{-1}$ show an appreciable difference between the perturbation advection over an impermeable wall than over a porous wall. On the other hand, the advection of a perturbation under the flow conditions of Willems *et al.* (2017) experiments and over both 3° and 7° half-angle cones lead to a marginal stabilization effect due to the low acoustic energy absorption coefficient of the C/C surface under such environment.

Figure 11 displays the homogeneous absorber theory predictions for the absorption coefficient β as a function of the wall pressure for both the experimental conditions of Wagner (2013), considering a 7°

TABLE IV. Operating conditions for the experiments performed by Willems *et al.* (2017).

Tunnel	Re_m (1/m)	M_∞ (–)	p_0 (Pa)	T_0 (K)	p_∞ (Pa)	T_∞ (K)	Condition
H2K	3.2×10^6	6.0	510	590	323	72	Noisy
H2K	4.1×10^6	6.0	510	500	323	61	Noisy
BAM6QT	2.4×10^6	5.8	212	422	165	55	Noisy
BAM6QT	3.3×10^6	5.8	294	424	229	55	Noisy
BAM6QT	2.3×10^6	6.0	225	427	143	52	Quiet
BAM6QT	7.2×10^6	6.0	694	420	439	51	Quiet
BAM6QT	9.5×10^6	6.0	928	424	587	52	Quiet
BAM6QT	11.5×10^6	6.0	1128	425	714	52	Quiet

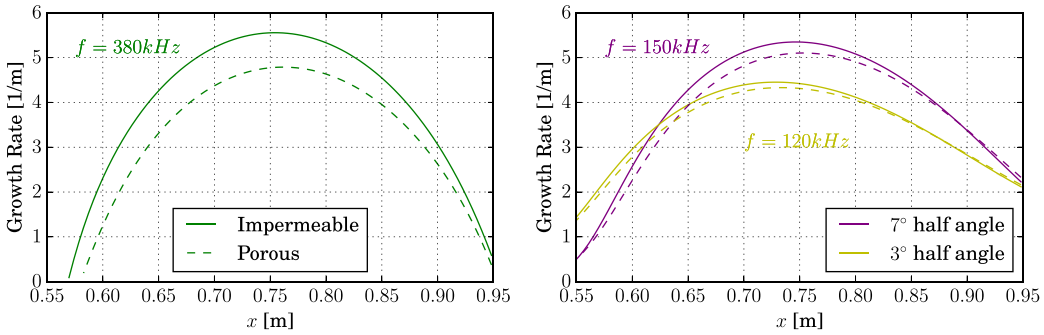

FIG. 10. Spatial growth rate of unstable boundary layer disturbance modes over impermeable and porous walls for two different experimental conditions and two different cone geometries. Left: flow conditions from Wagner *et al.* (2013) at $Re_m = 4.0 \times 10^6\ \mathrm{m}^{-1}$ on a 7° half angle cone. Right: flow conditions from Willems *et al.* (2017) at $Re_m = 9.5 \times 10^6\ \mathrm{m}^{-1}$ on a 3° and 7° half angle cones.

sharp cone, and Willems (2017), for both 3° and 7° sharp cones. It is clearly shown that the low pressures and frequencies that were encountered in the BAM6QT lead to a reduced acoustic energy absorption capability in comparison with the results obtained using the HEG wind tunnel. What may be interesting for design purposes is to study the minimum absorption coefficient needed for a considerable second-mode attenuation and consequent transition delay.

V. CONCLUSION

Numerical simulations regarding the influence of porous carbon-matrix ceramics on the stability of a hypersonic boundary layer were conducted to tackle three distinct objectives. First, simulations were carried out to analyze effects of an impedance boundary condition representative of a porous C/C surface on the second-mode instability in a hypersonic boundary layer at similar flow conditions as experiments performed in the HEG wind tunnel (Wagner *et al.*, 2013; Wagner, 2014; Wagner *et al.*, 2019). These experiments involved a 7° half-angle cone at a Mach number of 7.4 and reported a transition delay when a porous carbon/carbon (C/C) surfaces was present.

Within this objective, axisymmetric calculations were performed over impermeable and porous walls at different flow conditions and nose tip bluntness, in which the second-mode is excited via the application of a broadband pulse. Results show the presence of a porous surface representative of a C/C material increases the stability of a hypersonic boundary layer by both decreasing the growth rates in the region where the second-mode is unstable but also increasing its attenuation rates in the regions where it is stable. The current study represents a substantial advancement from the seminal work of Sousa *et al.* (2019) by utilizing a new spectral method for solving linear stability equations to calculate spatial growth rates and compare them with axisymmetric results. Additionally, the study expands its focus to include both sharp and blunt-nosed cones.

The process of recovery of a representative impedance curve from a porous material sample necessary to perform the aforementioned simulations is described in the Appendix; the acoustic absorption of the material was determined through experiments and these data were utilized in low-order models for reconstructing the real and imaginary components of the complex impedance across a broad frequency range. These curves are then fitted and represented as a finite sum of poles and residues pairs, and such representation is used as an input the time-domain impedance boundary condition (TDIBC) that models the effect of distributed surface porosity in the numerical computations.

The second objective was to understand the reasons behind the apparent ineffectiveness of a similar C/C porous surface in delaying transition at the experimental flow conditions reported by Willems *et al.* (2017). A linear stability study was performed and the results demonstrate that, at the conditions of the study, the decrease in the growth rate magnitude caused by the present of the C/C porous material was marginal and it was much smaller than the one predicted at

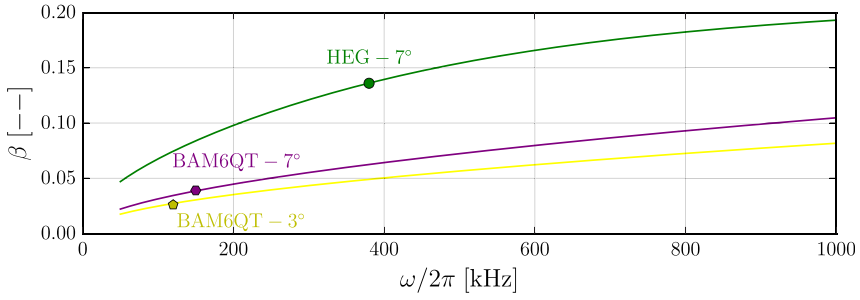

FIG. 11. Absorption coefficient (β) as a function of frequency for different wall pressure conditions corresponding to sharp cones at the experimental conditions reported by Wagner *et al.* (2013) and by Willems *et al.* (2017). For Wagner's experiments, the 7° half-angle cone at $Re_m = 4.0 \times 10^6\ \mathrm{m}^{-1}$ was used. For Willems' experiments, both a 3° half-angle cone and a hypothetical 7° cone were used for $Re_m = 9.5 \times 10^6\ \mathrm{m}^{-1}$. The symbols show what would be the magnitude of the acoustic absorption coefficient (β) for the most unstable frequency component at the aforementioned experimental conditions in the vicinity of $x \approx 0.75$ m.

the experimental conditions reported by Wagner *et al.* (2013). This behavior was attributed to the low pressure at the surface and a low frequency associated with the unstable disturbance band. It can be observed in the impedance education results gathered in the Appendix that the acoustic absorption of a C/C porous surface rapidly deteriorates at such conditions. Additionally, the gathered results show that the effectiveness of a C/C surface in dampening the unstable modes in the boundary layer increases asymptotically when the base pressure at the surface increases. To the authors' knowledge, the analysis gathered by tackling these first two objectives constitutes most complete study on the impact of C/C porous surfaces on a hypersonic boundary layers to date.

Finally, the third objective of this study has been to demonstrate that the current modeling approach, combining filtered compressible Navier–Stokes with broadband impedance boundary conditions, is appropriate for performing accurate three-dimensional simulations of the complete transition process. On that note, the TDIBC method enables the application of the impedance boundary to all frequencies simultaneously, providing a more comprehensive modeling capacity compared to previous studies, which were limited to a frequency-by-frequency analysis (Egorov *et al.*, 2008; Wang and Zhong, 2011; Lukashevich *et al.*, 2012). Additionally, transitional structures in a hypersonic boundary layer are capable of inducing the occurrence of steep gradients in the near-wall region and a dissipative scheme is necessary to stabilize the flow and reduce the resolution requirements in fully turbulent regions. Such a scheme would have to leave the second-mode instability untouched to be able to accurately predict the transition dynamics. In the current manuscript, we tested the sub-filter scale quasi-spectral viscosity (QSV) model developed in Sousa and Scalo (2022), which fulfills this non-trivial requirement. Despite not being necessary for the present axisymmetric simulations, this study employs the QSV model and achieves agreement between the axisymmetric simulations and linear stability results, indicating the QSV's suitability for three-dimensional transitional simulations.

ACKNOWLEDGMENTS

Victor Sousa and Carlo Scalo acknowledge the computational support of the Rosen Center for Advanced Computing (RCAC) at Purdue. Victor Sousa also acknowledges the support of the Lynn Fellowship administered by the interdisciplinary Computational Science and Engineering (CS&E) graduate program at Purdue University. This work was supported by the Air Force Office of Scientific Research Core and Young Investigator Program (C.S., Grant Nos. FA9550-16-1-0209 and FA9550-18-271-0292; A.W., Grant No. FA9550-16-1-0456).

AUTHOR DECLARATIONS

Conflict of Interest

The authors have no conflicts to disclose.

Author Contributions

Victor de Carvalho Britto Sousa: Formal analysis (equal); Investigation (equal); Methodology (equal); Software (equal); Validation (equal); Visualization (equal); Writing – original draft (equal). **Viola Wartemann:** Investigation (equal); Methodology (equal); Resources (equal). **Alexander Wagner:** Funding acquisition (equal); Investigation (equal); Methodology (equal); Resources (equal); Writing – review & editing (equal). **Carlo Scalo:** Conceptualization (equal); Funding acquisition (equal); Project administration (equal); Resources (equal); Software (equal); Supervision (equal); Writing – review & editing (equal).

DATA AVAILABILITY

The data that support the findings of this study are available from the corresponding author upon reasonable request.

APPENDIX: CHARACTERIZATION OF ACOUSTICALLY ABSORPTIVE POROUS CARBON-FIBER CERAMICS

1. Material development history

The porous carbon-fiber-reinforced carbon-matrix ceramic (C/C) used in the hypersonic transition delay experiments by the German Aerospace Center (DLR) (Wagner *et al.*, 2013; Wagner, 2014; Wagner *et al.*, 2019) (Fig. 12) represents an intermediate state of the manufacturing process of a material previously used as a Thermal Protection System (TPS) in the hypersonic flight experiment (SHEFEX) (Turner *et al.*, 2006; Weihs *et al.*, 2008). During the manufacturing process of such material, a green body composed of carbon fibers impregnated by a phenolic resin is pyrolyzed and the resin is converted to amorphous carbon (Krenkel, 2008). The carbon-fiber plies affect the contraction of the material in the cooling process, resulting in an anisotropic porous structure of the ceramic. This results in a pattern of small cracks elongated in the direction of the fibers, some of which propagate to the surface, lending the material its volumetric and surface porosity.

While the current manuscript will make use of acoustic absorption data solely deriving from this first generation porous C/C material, further improvements have been pursued by the DLR to obtain a new generation of acoustically absorptive material that can

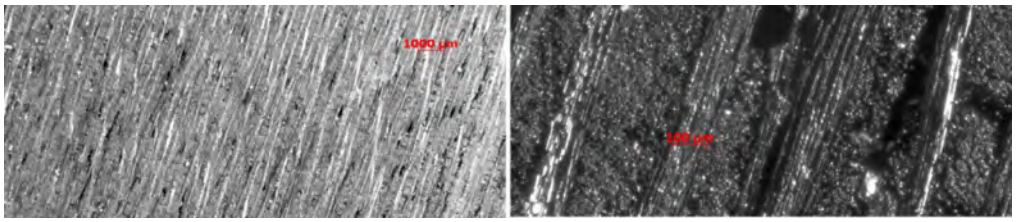

FIG. 12. Reflected-light microscopy generated images of the porous C/C material analyzed in this study showing a 1000 μm (left) and a 100 μm (right) scale.

also exhibit oxidation resistance and enhanced mechanical strength properties, bringing it closer to flight-ready TPS. Such improved properties are a consequence of a liquid silicone infiltration (LSI) process and subsequent reaction to SiC that, when performed on the first generation C/C material leads to the occlusion of all available pore space. A porous C/C-SiC material is obtained by replacing some carbon-fibers by a non-stable material capable of degrading during pyrolysis. This allows a higher intermediate porosity to be achieved and the LSI process to occur without complete pore obstruction (Dittert and Kütemeyer, 2017).

2. Impedance characterization

To model the effects of the porosity of the C/C sample in a cost-effective way in a high-fidelity simulation, its broadband acoustic absorption properties are imposed via a surface-averaged impedance boundary condition. The justification of the imposition of a spatially averaged, homogeneous impedance relies on the assumption that the characteristic length scales of the boundary layer instability waves and near-wall turbulence are much larger than the pore sizes of the C/C material. Wagner *et al.* (2013) determined the pore size distribution of the C/C by means of mercury intrusion porosimetry and concluded that approximately 80% of the relative pore volume is composed of pores with diameter smaller than 30 μm. Additionally, although there are large pores with diameter of the order of 100 μm, they compose only 1% of the relative pore volume. Therefore, the larger holes seen in the surface images of the C/C material (Fig. 12) do not have an important hydrodynamic effect. With the aforementioned pore size distribution, the surface-averaged impedance assumption is acceptable in regions of modal growth, where the wavelengths involved are of the order of several millimeters; however, some transitional and turbulent structures exhibit smaller scales, of the order of a fraction of a millimeter, which may be affected by microscale structure of the surface porosity. While this may start to challenge the validity of the surface-averaged impedance assumption, the results presented herein still produce valid insight on how realistic impedance levels affect the turbulent flow field and they allow a significant decrease in the computational cost that would be required to resolve very individual pore in a simulation.

In experimental acoustics, impedance is often measured via impedance tube testing, which is only effective up to ~8 kHz. However, the region of interest of the acoustic absorption of a C/C material is in the 100 kHz–1 MHz range at relatively low pressures (<10 kPa), which increases the difficulty of such measurements. Inspired by an innovation proposed by Fedorov *et al.* (2008), Wagner *et al.* (2014) designed a benchtop testing apparatus capable of performing ultrasonic characterization of the material. The absorption coefficient

$$\beta(\omega) = 1 - |\hat{R}(\omega)|^2 \tag{A1}$$

related to the acoustic power loss caused by thermoviscous dissipation inside the pores, was estimated by comparing the amplitude of ultrasonic waves reflected from the porous material A_{porous}, against a reference polished steel impermeable sample, A_{ref}, i.e., by evaluating the ratio $|\hat{R}| \sim A_{\text{porous}}/A_{\text{ref}}$ at various base pressures and discrete frequencies (Wagner *et al.* 2014). The reflection coefficient $\hat{R}(\omega)$ is, in turn, relatable to the complex impedance via

$$\hat{R}(\omega) = \frac{1 - Z_n(\omega)}{1 + Z_n(\omega)}. \tag{A2}$$

However, the complex nature of $\hat{R}(\omega)$ (not directly measured by the benchtest) also contains important information on the relative phase shift of the impinging and reflected waves, ultimately needed to extract an actual complex impedance value. Wagner *et al.* (2018) addresses the question of whether the benchtest setup could be used to measure such phase shift. He reported that, the minimum phase shift ($\angle\hat{R}$) resolution that could be measurable by this technique is approximately 2.2° for 125 kHz to 8.4° for 490 kHz. Since, the phase shift predicted by theoretical models (Fig. 14) is in the same range of the experimental uncertainty, only the absolute value of the reflection coefficient can be considered. Another important limitation of the benchtest setup is the fact that a sweep in the frequency parameter space, needed to accurately describe the impedance, would be unfeasible because each frequency measurement requires a specific transducer/receiver pair. This scenario leads to the conclusion that impedance analytical models, informed by the experimental data, are needed to ultimately characterize how the complex impedance varies in the frequency domain for the conditions of interest.

In this work, predictions of the surface averaged acoustic impedance are performed via the homogeneous absorber theory (HAT) described by Möser (2009) and used previously by Wagner (2014) to predict the C/C's behavior. A summary of this model can be found in Sousa *et al.* (2019). Other low-order impedance models that were developed for either regular-shaped holes (Fedorov *et al.*, 2001; Zhao *et al.*, 2020) or random porous structure (Fedorov *et al.*, 2003) exist but the model by Möser (2009) was the simplest and produced a satisfactory outcome. The results obtained analytically are then compared with experimental results of experimental acoustic characterization of ultrasonically absorptive porous samples (Wagner *et al.*, 2018).

These models are informed by physical parameters that characterize porous media and its influence on the flow through them such as: the porosity (ϕ), which is the ratio of the pore volume to the total volume; the flow resistivity (Ξ), that represents the resistance (pressure difference) to the flow of air through the medium; and the structure factor (κ), that accounts for the tortuosity of the porous structure. A complete description of these parameters can be found in Wagner *et al.* (2014).

In the current analysis, Ξ and κ were used as fitting parameters to minimize the difference between the modeled and measured value of β. The reason behind this is because κ cannot be measured or calculated directly for randomly structured porous materials. Although measurements for Ξ have been carried out at DLR, the approach of using flow resistivity as an optimization parameter was chosen here to improve the matching with the experiments. The goal is in fact for the present numerical simulations to follow as closely as possible the acoustic absorptions effects measured through a benchtop apparatus constructed by Wagner *et al.* (2014).

Figure 13 shows the measured absorption coefficient for the C/C sample with porosity $\phi = 0.15$ as a function of the base pressure for the different frequencies against the fitted model. The values

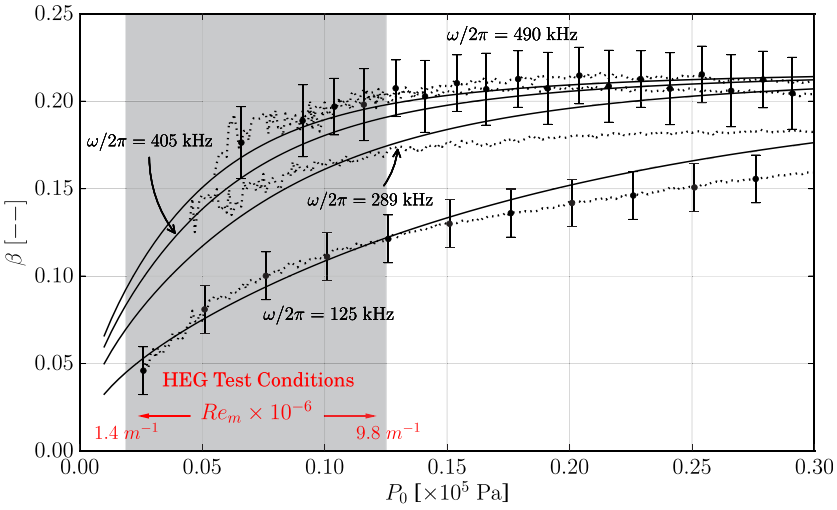

FIG. 13. Comparison between experimentally measured data (·····) for the absorption coefficient (β) of DLR's C/C sample with porosity $\phi = 0.15$ and the curve fit results based on the homogeneous absorption theory (——), with $\Xi = 13.6$ MPa s m^{-2} and $\kappa = 7.9$. A shaded region is included to highlight surface pressures achieved in Wagner *et al.* (2013) experiments on a 7°-half-angled cone. Error bars are included for benchtop data at frequencies of 125, 405, and 490 kHz.

obtained through the optimization procedure were $\Xi_{\mathrm{HAT}} = 13.64$ MPa s m^{-2}; $\kappa_{\mathrm{HAT}} = 7.94$. The results of the optimization for the flow resistivity, when compared with previously published results of $\Xi = 13.3$ MPa s m^{-2} (Wagner, 2014), agree well. In Sousa *et al.* (2019), a reference is made to new measurements of Ξ for the C/C sample that returned a value of 25.7 MPa, almost double of what was previously published. Initially it was thought that the difference was due to the better sealing of the samples on the new round of resistivity experiments but results from subsequent experiments have shown a dependency of the flow resistivity to the ambient pressure (Wagner *et al.*, 2019) and, for rarefied ambients, the value of $\Xi \approx 13$ MPa better represents the acoustic properties of the material.

It is worth noting that both the theoretical model and experiments predict relatively high levels of Ξ for the porous C/C. This results in a fairly thin layer of material, e.g., with a depth $H \approx 1$ mm, behaving as an infinite thickness absorber even in the low frequency range for this problem (≈ 100 kHz), i.e., interference patterns from a wave reflecting from the impermeable bottom end of the absorber are not present. This statement is made in the scope of the homogenous absorber theory that accounts for finite thickness effects with a correction term as

$$Z_{\mathrm{HAT}} = Z_\infty \frac{1 + e^{-j2k_a H}}{1 - e^{-j2k_a H}} \quad \text{and} \quad k_a = k\sqrt{\kappa}\sqrt{1 - j\frac{\Xi\phi}{\rho_0 \kappa \omega}}, \tag{A3}$$

where ϕ is the volume porosity, k and $\omega = 2\pi f$ are the wave number and angular frequency and ρ_0 the base density. Therefore, in the frequency range of interest, k_a is very large and the exponential terms of the correction factor decay rapidly to zero.

The pressure range of interest in the experiments conducted by Wagner *et al.* (2013) is shown in Fig. 13 as a shaded region. This is done by approximating the inviscid post-shock recovery pressure for a 7° sharp cone under the initial conditions using the Taylor–Maccoll equation and oblique shock relations. In this region, characterized by low pressures, the model follows the experimental data fairly well, losing accuracy at higher pressures.

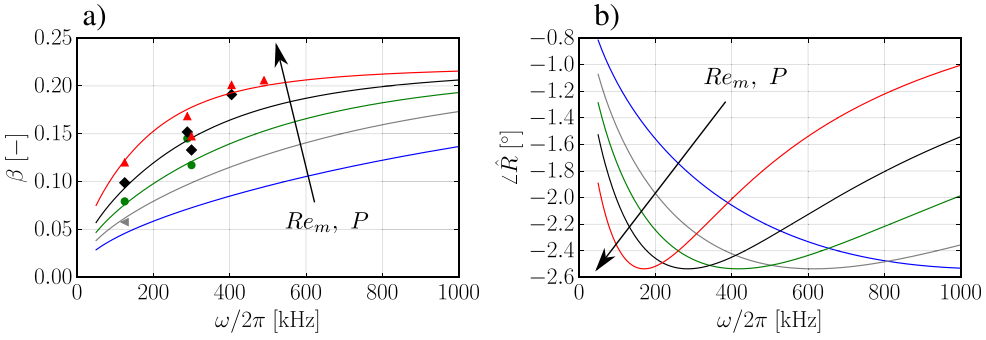

FIG. 14. Absorption coefficient (a) and phase difference between the incoming and reflected waves (b) as a function of frequency for various base pressures corresponding to different freestream Re_m achieved in HEG a 7° cone (see Table I for color scheme). Symbols (gray filled left triangle; green filled circle; black filled diamond; red filled triangle) show experimental data while lines (——) are the homogeneous absorber theory (HAT) predictions for $\phi = 0.15$, $\Xi = 13.6$ MPa s m^{-2} and $\kappa = 7.9$. As pressure decreases less experimental data are available due to the difficulty of measuring ultrasonic waves in rarefied environments.

Wave absorption data are presented as a function of pressure at various frequencies (Fig. 13) and vice versa (Fig. 14). The acoustic behavior of the C/C surface in the frequency domain is of critical importance since it directly affects the TDIBC introduced in the Navier–Stokes solver. Figure 14 shows β and the phase of the reflection coefficient ($\angle\hat{R}$) for five different pressures corresponding to the surface pressures that a sharp cone would experience under the five different Re_m reported in Table I. It shows that, as Re_m, and consequently pressure, increases, β also becomes higher. This correlates with the experimental findings of Wagner *et al.* (2013), who reported a higher transition delay capability of C/C ultrasonic absorbing surfaces for higher Re_m. The acoustic absorption coefficient seems to approach an asymptotic value at high frequencies but not enough experimental data are available to confirm this. The impedance mismatch between air and the vibrating piezoelectric component of the ultrasonic probes in fact increases with frequency and the degree of rarefaction, making benchtop measurements beyond 500 kHz and below ∼5 kPa very challenging.

REFERENCES

Chen, Y. and Scalo, C., "Effects of porous walls on near-wall supersonic turbulence," Phys. Rev. Fluids **6**, 084607 (2021a).

Chen, Y. and Scalo, C., "Trapped waves in supersonic and hypersonic turbulent channel flow over porous walls," J. Fluid Mech. **920**, A24 (2021b).

Chen, X., Zhu, Y., and Lee, C., "Interactions between second mode and low-frequency waves in a hypersonic boundary layer," J. Fluid Mech. **820**, 693–735 (2017).

Dittert, C. and Kütemeyer, M., "Octra—Optimized ceramic for hypersonic application with transpiration cooling," in *Advances in High Temperature Ceramic Matrix Compo sites and Materials for Sustainable Development; Ceramic Transactions* (John Wiley & Sons, 2017), Vol. 263, p. 389.

Douasbin, Q., Scalo, C., Selle, L., and Poinsot, T., "Delayed-time domain impedance boundary conditions (D-TDIBC)," J. Comput. Phys. **371**, 50–66 (2018).

Egorov, I. V., Fedorov, A. V., and Soudakov, V. G., "Receptivity of a hypersonic boundary layer over a flat plate with a porous coating," J. Fluid Mech. **601**, 165–187 (2008).

Fedorov, A. V., "Receptivity of a high-speed boundary layer to acoustic disturbances," J. Fluid Mech. **491**, 101–129 (2003).

Fedorov, A., "Transition and stability of high-speed boundary layers," Annu. Rev. Fluid Mech. **43**, 79–95 (2011).

Fedorov, A. and Tumin, A., "High-speed boundary-layer instability: Old terminology and a new framework," AIAA J. **49**, 1647–1657 (2011).

Fedorov, A. V., Kozlov, V., and Addison, R., "Reflection of acoustic disturbances from a porous coating of regular microstructure," AIAA Paper No. 2008-3902, 2008.

Fedorov, A. V., Kozlov, V. F., Shiplyuk, A. N., Maslov, A. A., and Malmuth, N. D., "Stability of hypersonic boundary layer on porous wall with regular microstructure," AIAA J. **44**, 1866–1871 (2006).

Fedorov, A. V., Malmuth, N. D., Rasheed, A., and Hornung, H. G., "Stabilization of hypersonic boundary layers by porous coatings," AIAA J. **39**, 605–610 (2001).

Fedorov, A., Shiplyuk, A., Maslov, A., Burov, E., and Malmuth, N., "Stabilization of a hypersonic boundary layer using an ultrasonically absorptive coating," J. Fluid Mech. **479**, 99–124 (2003).

Fung, K.-Y. and Ju, H., "Time-domain impedance boundary conditions for computational acoustics and aeroacoustics," Int. J. Comput. Fluid D. **18**, 503–511 (2004).

Gaster, M. and Grant, I., "An experimental investigation of the formation and development of a wave packet in a laminar boundary layer," Proc. R. Soc. London A **347**, 253–269 (1975).

Gautschi, W., "Gauss-Radau formulae for Jacobi and Laguerre weight functions," in *Computational Science, Mathematics, and Software: Proceedings of the International Symposium on Computational Science in Celebration of the 65th Birthday of John R. Rice*, West Lafayette, Indiana, 22–26 May, 1999 (Purdue University Press, 2002), Vol. 1, p. 237.

Gustavsen, B. and Semlyen, A., "Rational approximation of frequency domain responses by vector fitting," IEEE Trans. Power Delivery **14**, 1052–1061 (1999).

Hannemann, K., Martinez Schramm, J., Wagner, A., and Ponchio Camillo, G., "The high enthalpy shock tunnel Göttingen of the German aerospace center (DLR)," J. Large-Scale Res. Facil. JLSRF **4**, 1–14 (2018).

Jordan, S. A., "A large-eddy simulation methodology in generalized curvilinear coordinates," J. Comput. Phys. **148**, 322–340 (1999).

Kocian, T. S., "Computational hypersonic boundary-layer stability and the validation and verification of EPIC," Ph.D. thesis (Texas A&M University, 2018).

Krenkel, W., *Ceramic Matrix Composites: Fiber Reinforced Ceramics and Their Applications* (John Wiley & Sons, 2008).

Kroll, N. and Fassbender, J. K., "MEGAFLOW—Numerical Flow simulation for aircraft design: Results of the second phase of the German CFD initiative MEGAFLOW," *paper presented during Its Closing Symposium at DLR, Braunschweig, Germany, 10–11 December 2002* (Springer Science & Business Media, 2006), Vol. 89.

Lees, L., "Laminar heat transfer over blunt-nosed bodies at hypersonic flight speeds," J. Jet Propul. **26**, 259–269 (1956).

Lele, S. K., "Compact finite difference schemes with spectral-like resolution," J. Comput. Phys. **103**, 16–42 (1992).

Lin, J., Scalo, C., and Hesselink, L., "High-fidelity simulation of an ultrasonic standing-wave thermoacoustic engine with bulk viscosity effects," AIAA Paper No. 2017-0929, 2017.

Lukashevich, S., Morozov, S., and Shiplyuk, A., "Experimental study of the effect of a passive porous coating on disturbances in a hypersonic boundary layer 2. Effect of the porous coating location," J. Appl. Mech. Tech. Phys. **57**, 873–878 (2016).

Lukashevich, S., Maslov, A., Shiplyuk, A., Fedorov, A., and Soudakov, V., "Stabilization of high-speed boundary layer using porous coatings of various thicknesses," AIAA J. **50**, 1897–1904 (2012).

Mack, L., "Boundary-layer stability theory," Document No. 900-277 (Jet Propulsion Lab., Pasadena, CA, 1969).

Mack, L. M., "Boundary-layer linear stability theory," Report No. 709 (DTIC Document, 1984).

Mack, L. M., "On the inviscid acoustic-mode instability of supersonic shear flows," Theor. Comput. Fluid Dyn. **2**, 97–123 (1990).

Malik, M. L., "Numerical methods for hypersonic boundary layer stability," J. Comput. Phys. **86**, 376–413 (1990).

Malik, M., Zang, T., and Bushnell, D., "Boundary layer transition in hypersonic flows," in 2nd International Aerospace Planes Conference, 1990.

Malmuth, N., Fedorov, A., Shalaev, V., Cole, J., Hites, M., Williams, D., and Khokhlov, A., "Problems in high speed flow prediction relevant to control," AIAA Paper No. 1998-2695, 1998.

Morkovin, M., "Recent insights into instability and transition to turbulence in open-flow systems," Report No. 19880020695, August 1988; available at https://ntrs.nasa.gov/citations/19880020695.

Morozov, S., Lukashevich, S., Soudakov, V., and Shiplyuk, A., "Experimental study of the influence of small angles of attack and cone nose bluntness on the stabilization of hypersonic boundary layer with passive porous coating," Thermophys. Aeromech. **25**, 793–800 (2018).

Möser, M., *Engineering Acoustics: An Introduction to Noise Control* (Springer Science & Business Media, 2009).

Nagarajan, S., Lele, S. K., and Ferziger, J. H., "Leading-edge effects in bypass transition," J. Fluid Mech. **572**, 471–504 (2007).

Rasheed, A., Hornung, H. G., Fedorov, A. V., and Malmuth, N. D., "Experiments on passive hypervelocity boundary-layer control using an ultrasonically absorptive surface," AIAA J. **40**, 481–489 (2002).

Scalo, C., Bodart, J., and Lele, S. K., "Compressible turbulent channel flow with impedance boundary conditions," Phys. Fluids **27**, 035107 (2015).

Schneider, S. P., "Hypersonic laminar-turbulent transition on circular cones and scramjet forebodies," Prog. Aerosp. Sci. **40**, 1–50 (2004).

Shen, J., "Stable and efficient spectral methods in unbounded domains using Laguerre functions," SIAM J. Numer. Anal. **38**, 1113–1133 (2000).

Shen, J., Tang, T., and Wang, L.-L., *Spectral Methods: Algorithms, Analysis and Applications* (Springer Science & Business Media, 2011), Vol. 41.

Sivasubramanian, J. and Fasel, H. F., "Numerical investigation of the development of three-dimensional wavepackets in a sharp cone boundary layer at Mach 6," J. Fluid Mech. **756**, 600–649 (2014).
Softley, E., "Boundary layer transition on hypersonic blunt, slender cones," in 2nd Fluid and Plasma Dynamics Conference, 1969.
Sousa, V. C. B. and Scalo, C., "A unified quasi-spectral viscosity (QSV) approach to shock capturing and large-eddy simulation," J. Comput. Phys. **459**, 111139 (2022).
Sousa, V. C. B., Patel, D., Chapelier, J.-B., Wartemann, V., Wagner, A., and Scalo, C., "Numerical investigation of second-mode attenuation over carbon/carbon porous surfaces," J. Spacecr. Rockets **56**, 319–332 (2019).
Stetson, K. F., "Comments on hypersonic boundary-layer transition," Report No. WRD-TR-90-3057 (Wright Research and Development Center, 1990).
Taylor, G. I. and Maccoll, J., "The air pressure on a cone moving at high speeds.—I," Proc. R. Soc. London A **139**, 278–297 (1933).
Tritarelli, R., Lele, S., and Fedorov, A., "Stabilization of a hypersonic boundary layer using a felt-metal porous coating," J. Fluid Mech. **769**, 729–739 (2015).
Turner, J., Hoerschgen, M., Jung, W., Stamminger, A., and Turner, P., "SHEFEX—Hypersonic re-entry flight experiment vehicle and subsystem design, flight performance and prospects," AIAA Paper No. 2006-8115, 2006.
Wagner, A., "Passive hypersonic boundary layer transition control using ultrasonically absorptive carbon-carbon ceramic with random microstructure," Ph.D. thesis (Katholieke Universiteit, Leuven, 2014).
Wagner, A., Hannemann, K., and Kuhn, M., "Ultrasonic absorption characteristics of porous carbon–carbon ceramics with random microstructure for passive hypersonic boundary layer transition control," Exp. Fluids **55**, 1750 (2014).
Wagner, A., Kuhn, M., Schramm, J. M., and Hannemann, K., "Experiments on passive hypersonic boundary layer control using ultrasonically absorptive carbon–carbon material with random microstructure," Exp. Fluids **54**, 1606 (2013).
Wagner, A., Martinez Schramm, J., Dittert, C., Sousa, V., Patel, D. I., and Scalo, C., "Experimental and numerical acoustic characterization of ultrasonically absorptive porous materials," in Joint Thermophysics and Heat Transfer Conference, 2018.
Wagner, A., Wartemann, V., Dittert, C., and Kütemeyer, M., "Passive hypersonic transition control by means of ultrasonically absorptive thermal protection materials (UAT)," Report No. AFRL-AFOSR-UK-TR-2025-0025 (DTIC, 2019).
Wagner, A., Wartemann, V., Kuhn, M., Dittert, C., and Hannemann, K., "The potential of ultrasonically absorptive TPS materials for hypersonic vehicles," AIAA Paper No. 2015-3576, 2015.
Wang, X. and Zhong, X., "The impact of porous surface on hypersonic boundary layer instability," AIAA Paper No. 2010-5021, 2010.
Wang, X. and Zhong, X., "Phase angle of porous coating admittance and its effect on boundary-layer stabilization," AIAA Paper No. 2011-3080, 2011.
Wartemann, V., Wagner, A., Giese, T., Eggers, T., and Hannemann, K., "Boundary-layer stabilization by an ultrasonically absorptive material on a cone in hypersonic flow: Numerical investigations," CEAS Space J. **6**, 13–22 (2014).
Wartemann, V., Wagner, A., Kuhn, M., Eggers, T., and Hannemann, K., "Passive hypersonic boundary layer transition control using an ultrasonically absorptive coating with random microstructure: Computational analysis based on the ultrasonic absorption properties of carbon-carbon," Procedia IUTAM **14**, 413–422 (2015).
Weihs, H., Longo, J., and Turner, J., "The sharp edge flight experiment SHEFEX II, a mission overview and status," AIAA Paper No. 2008-2542, 2008.
Willems, S., Gülhan, A., Ward, C. A., and Schneider, S. P., "Free transition on a slender cone in a quiet and a conventional wind tunnel and the effect of ultrasonically absorptive materials," Prog. Flight Phys. **9**, 497–516 (2017).
Zhao, R., Zhang, X., and Wen, C., "Theoretical modeling of porous coatings with simple microstructures for hypersonic boundary-layer stabilization," AIAA J. **58**, 981–986 (2020).
Zhu, W., Chen, X., Zhu, Y., and Lee, C., "Nonlinear interactions in the hypersonic boundary layer on the permeable wall," Phys. Fluids **32**, 104110 (2020).